DESIGNING AND TESTING CONTROL SURFACES WITH PLASMA ACTUATORS

A THESIS SUBMITTED TO
THE SCHOOL OF GRADUATE STUDIES
OF
UNIVERSITY OF TURKISH AERONAUTICAL ASSOCIATION

BY

MEHMET ÇALIKOĞLU

IN PARTIAL FULFILLMENT OF THE REQUIREMENTS
FOR
THE DEGREE OF MASTER OF SCIENCE
IN
AEROSPACE ENGINEERING

JUNE 2025

DESIGNING AND TESTING CONTROL SURFACES WITH PLASMA ACTUATORS

A THESIS SUBMITTED TO
THE SCHOOL OF GRADUATE STUDIES
OF
UNIVERSITY OF TURKISH AERONAUTICAL ASSOCIATION

BY

MEHMET ÇALIKOĞLU

IN PARTIAL FULFILLMENT OF THE REQUIREMENTS
FOR
THE DEGREE OF MASTER OF SCIENCE
IN
AEROSPACE ENGINEERING

SUPERVISOR: Assoc. Prof. Dr. Mecit YAMAN

JUNE 2025

Approval of the thesis:

DESIGNING AND TESTING CONTROL SURFACES WITH PLASMA ACTUATORS

Submitted by **MEHMET ÇALIKOĞLU** in partial fulfillment of the requirements for the degree of **Master of Science in Aerospace Engineering, University of Turkish Aeronautical Association** by,

Assoc. Prof. Dr. Adnan GÜZEL
Dean, The School of Graduate Studies,
University of Turkish Aeronautical Association _____

Prof. Dr. Uğur Murat LELOĞLU
Head of The Department, Aerospace Engineering,
University of Turkish Aeronautical Association _____

Assoc. Prof. Dr. Mecit YAMAN
Supervisor: Aeronautical Engineering,
University of Turkish Aeronautical Association _____

Examining Committee Members:

Prof. Dr. Çetin ŞENTÜRK
Aeronautical Engineering,
University of Turkish Aeronautical Association _____

Assoc. Prof. Dr. Mecit YAMAN
Aeronautical Engineering,
University of Turkish Aeronautical Association _____

Assoc. Prof. Dr. Özgür KELEKÇİ
Electrical and Electronics Engineering,
University of Turkish Aeronautical Association _____

Assoc. Prof. Dr. Mustafa KAYA
Aerospace Engineering,
Ankara Yıldırım Beyazıt University _____

Asst. Prof. Dr. Zeynel DEPREM
Electrical and Electronics Engineering,
University of Turkish Aeronautical Association _____

Date: 23.06.2025

I hereby declare that all information in this document has been obtained and presented in accordance with academic rules and ethical conduct. I also declare that, as required by these rules and conduct, I have fully cited and referenced all material and results that are not original to this work.

Name, Last name : Mehmet Çalıkoğlu

ABSTRACT

DESIGNING AND TESTING CONTROL SURFACES WITH PLASMA ACTUATORS

Çalıkoğlu, Mehmet
M.S., Department of Aerospace Engineering,
Supervisor: Assoc. Prof. Dr. Mecit Yaman

June 2025, 71 pages

The control surfaces of aircraft manipulate the airflow to perform the desired maneuvers (e.g. rolling, yawing and pitching), and these systems consist of moving parts. The aim of this study is to investigate the feasibility of using a solid-state maneuvering system as a replacement for conventional control surfaces. The plasma thrust system is designed with asymmetric and concentric positioning of two electrodes (emitter and collector) and produces thrust by ionizing the air under high voltage (~40kV). Unlike conventional control surfaces, this system does not have moving parts, offering certain advantages. These advantages include reducing the weight of the aircraft, eliminating noise pollution, and simplifying the mechanical design. To test the feasibility of this system, experiments were performed, and test setups were prepared to obtain the necessary data. Thrust measurements were conducted at varying electrode distances using a high-precision laboratory scale to ensure accurate thrust quantification. And, speed measurements were performed using a rotating rod apparatus, which revolved around its own central axis. It was found that thrust and speed generally increased in direct proportion to the power. The effect of the distance between the electrodes on the thrust produced was also tested. For the model used, the optimal electrode distance was determined to be approximately 15mm, thrust value obtained is 7.82 mN. The calculated results consistent with this value are as follows: thrust density(ø) = 6.89 N/m² and thrust to power ratio(Θ) = 0.72 N/kW. When compared with previous studies, particularly the one conducted [4], these values

were obtained: ø = 3 N/m² and Θ = 6.25 N/kW. The optimum voltage and current values at which the system operates were also determined by speed testing, and the optimum values was determined to be 5V and 3A, respectively. The efficiency of this system is 0.04%.

Keywords: Thrust, Plasma actuator, Control surface, Ionic wind

ÖZ

PLAZMA AKTÜATÖRLER İLE KONTROL YÜZEYLERİ TASARLAMA VE TEST EDİLMESİ

Çalıkoğlu, Mehmet
Yüksek Lisans, Havacılık ve Uzay Mühendisliği
Tez Yöneticisi: Doç. Dr. Öğr. Üye. Mecit Yaman

Haziran 2025, 71 sayfa

Uçakların kontrol yüzeyleri, istenen manevraları (örneğin yatış, yunuslama ve sapma ve hareketleri) gerçekleştirmek amacıyla hava akımını manipüle eder ve bu sistemler hareketli parçalardan oluşur. Bu çalışmanın amacı, geleneksel kontrol yüzeylerinin yerine katı hâl (solid-state) bir manevra sisteminin kullanılabilirliğini araştırmaktır. Plazma itki sistemi, iki elektrotun (emitter ve collector) asimetrik ve eşmerkezli konumlandırılmasıyla tasarlanmış olup, yüksek gerilim (~40kV) altında havayı iyonlaştırarak itki üretir. Geleneksel kontrol yüzeylerinden farklı olarak, bu sistemde hareketli parçalar bulunmamaktadır ve bu durum bazı avantajlar sunmaktadır. Bu avantajlar arasında uçağın ağırlığının azaltılması, gürültü kirliliğinin ortadan kaldırılması ve mekanik tasarımın sadeleştirilmesi yer almaktadır. Sistemin uygulanabilirliğini test etmek amacıyla deneyler gerçekleştirilmiş ve gerekli verilerin elde edilmesi için test düzenekleri hazırlanmıştır. İtki ölçümleri, farklı elektrot mesafelerinde yüksek hassasiyetli bir laboratuvar terazisi kullanılarak gerçekleştirilmiş ve hassas ölçüm ile itki değerleri elde edilmiştir. Hız ölçümleri ise kendi merkezi etrafında dönen bir çubuk düzeneği yardımıyla yapılmıştır. Yapılan ölçümler sonucunda, itki ve hızın genel olarak güçle doğru orantılı olarak arttığı görülmüştür. Elektrotlar arasındaki mesafenin üretilen itki üzerindeki etkisi de test edilmiştir. Kullanılan model için optimum elektrot mesafesi yaklaşık 15 mm olarak belirlenmiş, elde edilen itki değeri ise 7.82 mN'dur. Bu değere karşılık gelen hesaplanan sonuçlar ise şu şekildedir: itme yoğunluğu(ø)=6.89 N/m² ve itme-

güç(Θ)=0.72 N/kW. Önceki çalışmalarla, özellikle[4] numaralı çalışmayla karşılaştırıldığında, şu değerlere ulaşılmıştır: ø=3 N/m² ve Θ=6.25 N/kW. Sistemin çalıştığı optimum voltaj ve akım değerleri de hız testleriyle belirlenmiş ve bu değerler 5V ve 3A olarak tespit edilmiştir. Bu sistemin verimi ise %0.04 olarak hesaplanmıştır.

Anahtar kelimeler: İtme, Plazma aktüatör, Kontrol yüzeyi, İyonik rüzgâr

ACKNOWLEDGMENTS

I would like to express my deepest gratitude to my advisor, Assoc. Prof. Dr. Mecit Yaman, for his invaluable guidance, insightful advice, constructive criticism, continuous encouragement, and thoughtful suggestions throughout the course of this research.

I would also like to extend my heartfelt thanks to my family for their unwavering support, endless patience, and encouragement throughout my life. Their upbringing and constant presence have been a source of strength and motivation during my academic journey.

TABLE OF CONTENTS

LIST OF TABLES

LIST OF FIGURES

LIST OF SYMBOLS

EAD: Electro-aerodynamic
a: Radius of the wire
A: Discharge cross-section
C_D: Drag Coefficient
δ: Ionization region
d: Inter electrode distance
DBD: Dielectric-Barrier-Discharge
E: Electric field strength
e: Unit charge
$\bar{E}$: Average Electric field strength
EGD: Electrogasdynamic
EHD: Electrohydrodynamic
ESPs: Electrostatic precipitators
HAPS: High-Altitude Pseudo-Satellite
I: Discharge current
j: Current density
λ: Traveled the distance
m: Mass
N: Total number of ions in the discharge
n_i: Product of ion density
Ø: Thrust density ratio
P: Power
P_{input}: Input Power
θ: Thrust to power ratio
r: Radius
S: Wing Area
T: Thrust generated by the ionic wind
V: Electric potential
v: Velocity
v_i: average ion velocity
x: Distance along the coordinate direction
η: Power efficiency
μ: Ion mobility

CHAPTER 1

INTRODUCTION

1.1 Problem Statement

The control surfaces are essential components for aircraft because they can enable necessary maneuvers by manipulating airflow. Conventional control surfaces have complex systems, so they have many disadvantages such as avionics problems, maintenance requirements, structural problems and noise problems because they have moving components. An example of conventional control surfaces is shown in Figure 1.1.

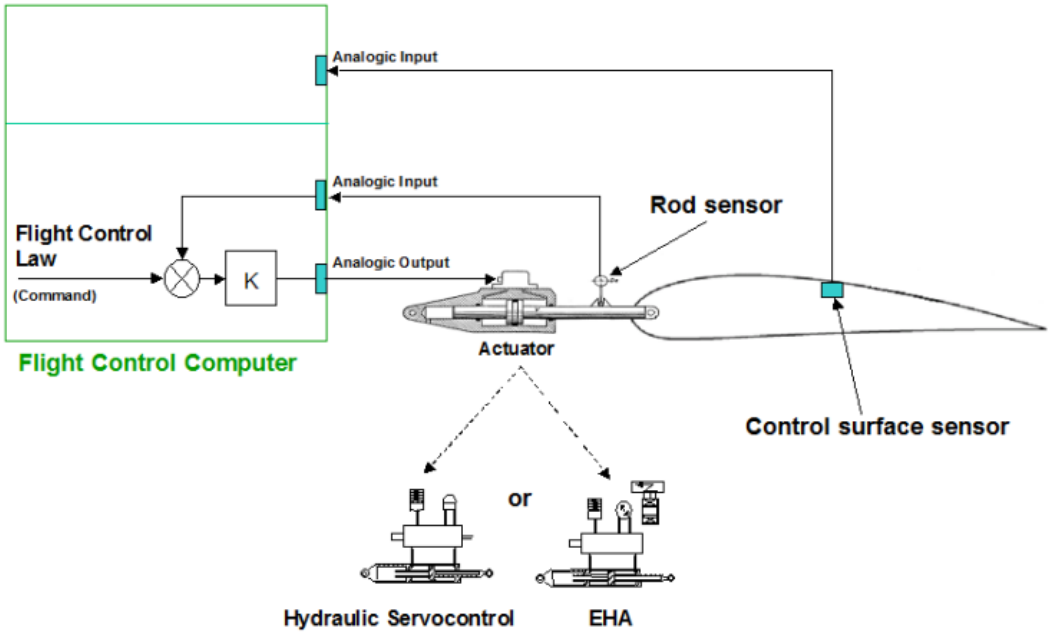

Figure 1.1 Block Diagram of the Example Conventional Control Surface[40].

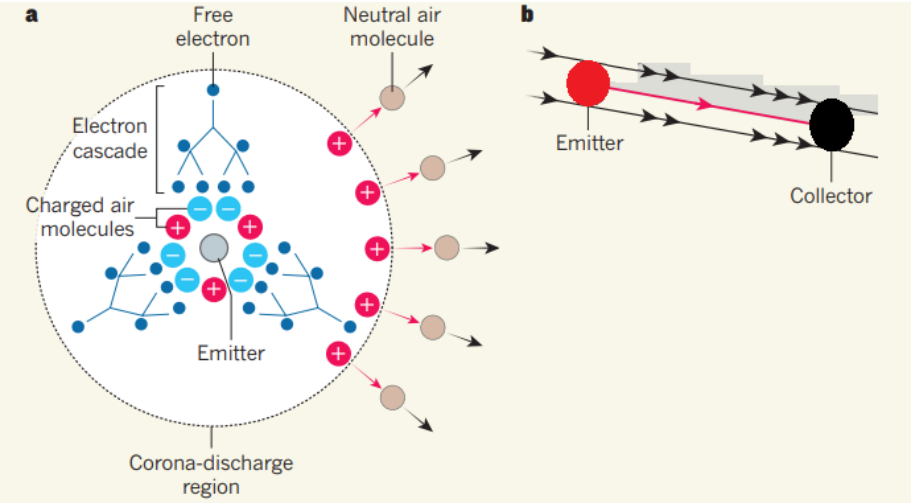

Figure 1.2 Schematic illustration of ionic wind generation and propulsion mechanism. (a) A high electric field near the emitter wire initiates a corona discharge, producing charged air molecules that drift away and collide with neutral air, creating an ionic wind. (b) The aircraft uses arrays of emitters and collectors, where the charged particles flow between them (red arrows), accelerating neutral air (black arrows) to generate thrust [39].

Solid-state refers to devices or systems that operate using solid materials, typically without any moving parts or fluids. In electronics, it describes components composed entirely of solid substances such as semiconductors instead of mechanical elements or vacuum tubes. Applied to propulsion, a solid-state system generates thrust through the movement of ions rather than mechanical components. A solid-state propulsion system produces ionic wind also known as corona wind between two electrodes. Ionic wind is generated in atmospheric air when a high voltage is applied between two asymmetrically sized electrodes, typically in a wire-to-cylinder configuration. In this setup, the smaller electrode referred to as the emitter produces an electric field that exceeds the breakdown strength of air (approximately 3 MV/m), enabling electrons to gain sufficient energy to ionize nearby air molecules. The positively charged electrode, called the emitter, can carry either a positive or negative charge, while the opposing collector electrode is grounded. By applying high voltage, the air between the electrodes is ionized, and the resulting ionized airflow, due to the electric field, creates thrust in the direction opposite to the flow. An illustration of the plasma propulsion system is provided in Figure 1.2. In a study conducted in 2018, an aircraft equipped

entirely with a solid-state propulsion system was successfully flown [4]. The phenomenon behind this mechanism is corona discharge, which can induce a pressure gradient, fluid velocity, or both within the host dielectric medium, depending on the system configuration. The earliest documented investigation of pressure gradient formation via corona discharge is attributed to [38] in 1899. Since then, numerous studies have examined the generation of both pressure differentials and fluid motion as a result of this effect. While many earlier investigations primarily focused on liquid dielectrics, subsequent research expanded into aerodynamic power generation through corona discharge. This led to the development of performance equations largely independent of system geometry. One study explored the corona wind effect in air under a zero-pressure gradient condition. The model assumed that velocity starts at zero at the emitter and reaches a maximum at the collector. However, this assumption introduced a transverse velocity component, which was inconsistent with the one-dimensional nature of the model. Another line of research examined Electrogasdynamic (EGD) channel flows in lightly ionized gases, although the results were found to be inapplicable to low-speed ion-neutral propulsion systems. Beyond theoretical investigations, practical devices employing corona wind for thrust generation have also been developed and tested in recent years.

The objective of this study is to replace the control surfaces with a solid-state propulsion system. The rudder, as a control surface, generates a higher moment with less force due to its distance from the center of gravity compared to other control surfaces. By eliminating the rudder, the vertical stabilizer can also be removed, reducing aerodynamic drag caused by this component because the surface area will reduce. Because drag force is directly proportional to surface area, see (1.1).

Aerodynamic drag force is represented by D, and it depends on air density (ρ_{air}), air velocity (V_{inf}), drag coefficient (C_D) and surface area (S).

$$D = \frac{1}{2}\rho_{air} V_{inf}^2 C_D S \tag{1.1}$$

The thrust force of the plasma thrust system is not dependent on the area, as shown in (1.2). Ion mobility is a measure of how quickly an ion moves through a medium under the influence of an electric field. It is defined as the drift velocity of the ion per unit electric field strength. It represents by μ. I represent the current. Distance between electrodes is represented by d. Thrust force is:

$$T = I\frac{d}{\mu} \tag{1.2}$$

Therefore, optimized designs can be created by minimizing the drag force. Additionally, this approach allows for the integration of control mechanisms at the wingtips instead of the tail, enabling them to function as winglets, mitigating vortex formation, and serving as a fail-safe system through asymmetric operation. This modification aims to enhance efficiency, simplify the control mechanism, and provide new design opportunities for both commercial and military aviation. Two different design concepts are shown in Figure 1.3.

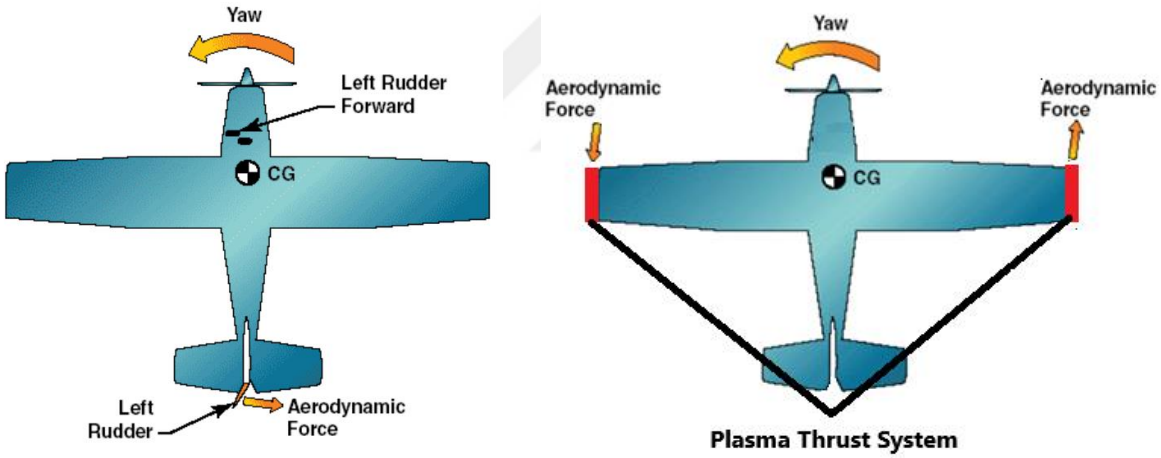

Figure 1.3 Rudder System / Plasma Thrust System

1.2 Contributions

Here are the contributions of this study: This work first aims to demonstrate the existence of ionic wind using a visual experimental setup. It then establishes a thrust

measurement system intended to reveal the relationship between power input and generated thrust, along with identifying the optimum electrode distance. Finally, a mechanical setup is designed to test the actuator's ability to generate motion, enabling the evaluation of efficiency and thrust-to-power ratio in subsequent analyses.

1.2.1 Ionic wind demonstration using appropriate setup

In the initial phase of this study, the primary objective was to demonstrate the presence of airflow. To achieve this, an experimental setup was designed to allow visual observation. In chapter 3, the experimental setups are explained and in chapter 4, the results are included.

1.2.2 Thrust measurement

The second phase of this study involves the establishment of a measurement system to quantify the generated thrust, followed by the collection of results and the demonstration of the linear relationship between the applied power and the resulting thrust using graphical analysis. And the optimum electrode distance is determined as a result of these tests and the next phase is designed according to this information. In chapter 3, the experimental setups are explained and in chapter 4, the results are included.

1.2.3 Demonstrated mechanical action

The final phase is the design of the EAD thrust system placed on a rod that moves with the help of bearings. Then, the optimum operating range is determined according to the different current and voltage values applied, and the efficiency and thrust-power ratio are calculated by showing that the system can move. In chapter 3, the experimental setups are explained and in chapter 4, the results are included.

CHAPTER 2

LITERATURE REVIEW

Electroaerodynamic (EAD) propulsion, also known as ionic wind propulsion, has gained attention for its potential applications in low emission and noise reducing propulsion systems. This chapter provides an overview of key studies and findings relevant to the development and optimization of EAD-based systems, with a focus on ionic wind generation and its applications in aviation.

2.1 Flight of an aeroplane with solid-state propulsion

In the broader context of EHD propulsion, several studies have addressed the challenges and opportunities associated with its implementation. For example, one investigation [1] explored the practicality of ionic wind engines, concluding that while they may not be suitable for large-scale aircraft propulsion, they hold promises for specialized applications such as solar-powered UAVs.

2.2 An Investigation of Ionic Wind Propulsion

Another critical study demonstrated the feasibility of solid-state propulsion, achieving thrust-to-power ratios comparable to conventional jet engines under specific configurations [4]. This study serves as the primary reference for this research, as it employs similar voltage levels and electrode arrangements.

Thickness(mm) of ionization region is given by

$$\delta = \sqrt{a} \tag{2.1}$$

Where a represents the radius of wire. The unit thrust is the force generated by a single ion in electrical field. It is represented by T_i.

$$T_i = eE \tag{2.2}$$

Unit charge is represented by e and electrical field represented by E. The total thrust force is obtained by multiplying the number of ions by the unit thrust.

$$T = NT_i = NeE \tag{2.3}$$

Total number of ions is represented by N. The discharge current is given by

$$I = n_i e v_i A \tag{2.4}$$

Product of ion density is represented by n_i, average ion velocity is represented by v_i and collector electrode area is represented by area.

The ion drift velocity is given by

$$v_i = \mu E \tag{2.5}$$

Ion mobility (m^2/V-sec) is a measure of how quickly an ion moves through a medium (usually a gas or liquid) under the influence of an electric field. It is defined as the drift velocity of the ion per unit electric field strength. It is represented by μ. I(amps) represents current. The ion mobility of air, for example, is relatively low and changes with humidity—ranging from approximately ($2.15\times10^{-4}m^2$/V) in dry conditions to 1.60×10^{-4} m^2/V) in saturated air.

The thrust calculation is given by

$$T = NeE = \frac{N}{V}\, eE(Ad) = neE(Ad)$$
$$= \frac{(n_i e v_i A)E(Ad)}{v_i A} = \frac{I\, E\, d}{\mu\, E} \qquad (2.6)$$
$$= \frac{Id}{\mu}$$

Distance between electrodes is represented by d. The thrust-to-power ratio depends on the electric field, thrust-to-power ratio is given by

$$\Theta = \frac{T}{P} = \frac{\frac{Id}{\mu}}{(IV)} = \frac{1}{(\mu E)} \qquad (2.7)$$

Efficiency represents how much of the electrical energy entering the system is converted into thrust. Efficiency is given by

$$\eta = \frac{P_{output}}{P_{input}} = \frac{T\, v}{P} \qquad (2.8)$$

The thrust is represented by T, v represents speed and P represents power.

Constant acceleration is given by

$$a = \frac{eE}{m_i} \qquad (2.9)$$

Mass of ion is represented by m_i. The traveled distance is given by

$$\lambda = \frac{at^2}{2} \qquad (2.10)$$

Time is represented by t. The average speed is given by

$$v_i = \frac{\lambda}{t} = \frac{at}{2} = \frac{eE}{2m_i}\sqrt{\frac{2m_i\lambda}{eE}} = E\sqrt{\frac{e\lambda}{2m_iE}} \tag{2.11}$$

Ion mobility is given by

$$\mu = \sqrt{\frac{e\lambda}{2m_i\,E}} \tag{2.12}$$

Force accelerating the air is given by

$$F = \frac{2nm_i\,v_i\,d}{\lambda} = Id\sqrt{\frac{2m_i\,E}{e\lambda}} = \frac{Id}{\mu} \tag{2.13}$$

Therefore F = T.

2.3 Electrohydrodynamic ionic wind, force field, and ionic mobility in a positive dc wire-to-cylinders corona discharge in air

One of the foundational works in this domain is the study of ionic wind generation by a wire-cylinder configuration under atmospheric conditions. This research highlights the impact of variables such as voltage and electrode spacing on thrust-to-power ratios and efficiency, offering insights into optimal configurations [6].

2.4 Ionic wind generation by a wire-cylinder-plate corona discharge in air at atmospheric pressure

Similarly, a study on corona discharge in wire-to-cylinder systems emphasizes the role of electrode geometry and electric field intensity in optimizing ionic mobility

and thrust density [9]. These findings align closely with the configuration employed in this research.

2.5 Characterization of ionic wind velocity

Quantitative characterization of ionic wind remains an ongoing challenge due to measurement limitations. Traditional tools, such as Pitot tubes, often fail to capture low-speed flows accurately, necessitating alternative approaches like particle image velocimetry or hot wire anemometry [11]. These methods provide valuable data for validating computational models and optimizing experimental setups.

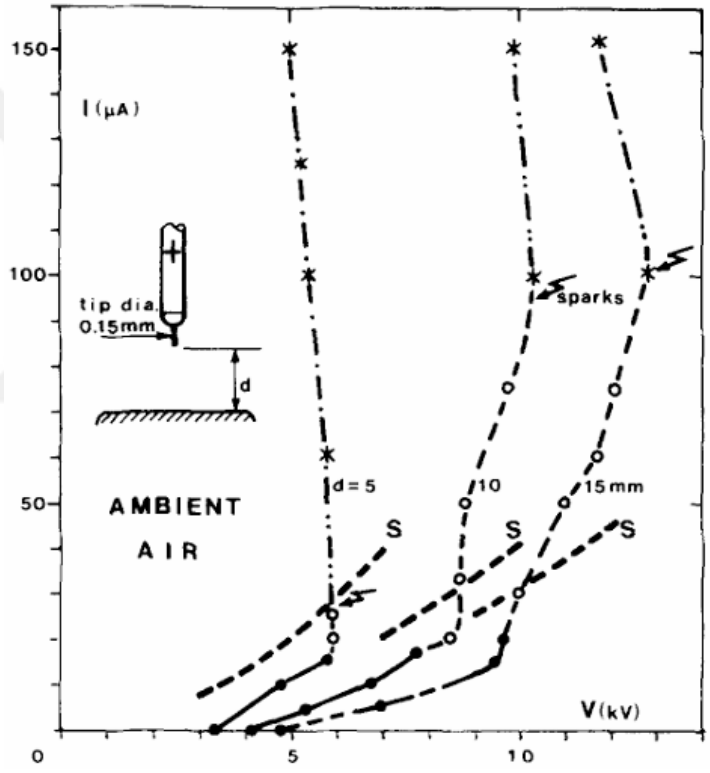

Figure 2.1 Current–voltage characteristics for positive point-to-plane coronas in ambient air. Only streamer and streamer-spark coronas are observed at currents exceeding the unipolar space-charge saturation limits [17].

Symbols and curves represent:

- **Dots with solid lines:** Positive glow corona
- **Circles with dashed lines:** Streamer corona

- **Quotation marks with dash-dot-dot lines:** Streamers with intermittent sparks
- **Asterisks with dash-dot lines:** Periodic streamer-spark corona
- **Curves labeled 'S':** indicate the unipolar space-charge saturation current limits ($\mu = 2.1 \times 10^{-4}$ m²/V·s).

In summary, the existing literature underscores both the potential and limitations of EHD propulsion. While challenges such as efficiency and scalability persist, advancements in electrode design, thrust density optimization, and measurement techniques continue to drive innovation in this field. This study builds upon these foundations by focusing on the integration of EHD systems into aircraft control surfaces, leveraging insights from prior research to address specific design and performance criteria.

2.6 Electrohydrodynamic thrust density using positive corona-induced ionic winds for in-atmosphere propulsion

Efficiency remains a pivotal challenge in EHD propulsion. The trade-off between thrust-to-power ratio and thrust density has been a recurring theme in literature. Experimental studies suggest that while increased power input can enhance thrust density, it often leads to reduced energy efficiency. Advanced configurations, such as multi-stage electrode systems, have been proposed to address these limitations, achieving a balance between thrust density and energy consumption [12].

2.7 Ion-Neutral Propulsion in Atmospheric Media

A foundational theoretical and experimental study has been conducted on aerodynamic corona discharge propulsion systems, providing insights into their underlying physical mechanisms and performance limitations. The investigation utilizes a one-dimensional, constant-area analytical model that incorporates multiple point, space-charge-limited emission of negative ions. Within this framework, explicit expressions for system performance parameters are derived. Experimental validation supports the

theoretical predictions, confirming that the energy conversion efficiency from electrical input to propulsive output is approximately 1%. The majority of the energy input is observed to be dissipated as heat, indicating significant thermal losses inherent in the current system configuration. Among various influencing parameters, ion mobility emerges as the most critical factor affecting performance [16].

2.8 Simple approximate treatment of unipolar space-charge-dominated coronas: The Warburg law and the saturation current

Ionic thrust is a variable that depends on the distance between the electrodes. It emphasizes the importance of optimum distance. For this reason, an example of the analysis made to find the optimum distance, is shown in Figure 2.1 [17].

2.9 A Comprehensive Review of Atmosphere-Breathing Electric Propulsion Systems

In addition to propulsion, ionic wind technology has been explored for control surface applications. For example, studies on rudder optimization have demonstrated the potential for integrating EHD systems into aircraft control mechanisms, highlighting structural and aerodynamic advantages [13][14]. These insights are particularly relevant for the design goals of this research, which aim to develop an EHD-based control surface rather than a primary propulsion system.

In recent years, atmosphere-breathing electric propulsion (ABEP) systems have attracted increasing interest for low Earth orbit (LEO) missions due to their potential to utilize ambient atmospheric particles as propellant. This approach enables thrust compensation, thereby extending spacecraft operational lifetimes. Various studies have explored different ABEP concepts and compared several types of electric propulsion technologies to identify those best suited for atmosphere-breathing applications. A detailed evaluation of different thruster types highlights their respective characteristics and limitations. Prior research also provides performance

data that could serve as a foundation for future developments. However, significant challenges remain, including intake efficiency, power requirements for ionization, and electrode degradation, which currently hinder the practical application of ABEP systems in space environments [18].

2.10 An empirical model for ionic wind generation by a needle-to-cylinder dc corona discharge

An experimental investigation was conducted to analyze ionic wind generation using a needle-to-cylinder DC corona discharge configuration. The study focused on how ionized gas molecules, accelerated by a strong electric field, induce airflow along electric field lines. Key parameters such as electrode geometry, inter-electrode distance, and applied voltage were varied to observe their effects on ionic wind velocity and discharge current. Based on the measurements, the authors proposed an empirical model relating wind velocity to electrode design and voltage, offering valuable insight for the optimization of ionic wind cooling systems in compact electronic devices [19].

2.11 Basic study on flow control by using plasma actuator

A plasma actuator utilizing DC corona discharge has been developed for active flow control under atmospheric temperature and pressure conditions. The actuator, consisting of a sharp pin electrode and a grounded plate, generated an electrohydrodynamic (EHD) wind, with airflow velocities reaching up to 2 m/s as measured by a hot-wire anemometer. Diagnostic analysis included emission spectra, electrical characteristics (voltage, current, power), and ozone concentration. Results indicated that increasing the discharge voltage enhanced flow velocity, though a saturation point was eventually reached. This study demonstrates the effectiveness of EHD-induced flow modification over flat surfaces, supporting its potential use in flow control applications [20].

2.12 Corona discharge in wind for electrically isolated electrodes

Investigation corona discharge behavior under wind for electrically isolated electrodes, relevant to airborne systems. Wind affects corona in two competing ways: by enhancing ion removal with increasing current and by causing negative charging with reducing current. Three discharge regimes were identified, showing that classical scaling laws do not fully apply to isolated systems. The results highlight the potential for using glow corona in the wind for controlled charging of floating structures [21].

2.13 Electro-hydrodynamic (EHD) thrust analysis in wire-cylinder electrode arrangement

A prototype converter was built based on the proposed optimization strategy and successfully integrated into an EAD propulsion system for a small unmanned aerial vehicle (UAV). Beyond the field of EAD propulsion, the research offers broader implications for the design of compact and lightweight high-voltage converters in other weight-sensitive applications, such as aerospace systems and portable power electronics.

A study was conducted on thrust generation via the electro-hydrodynamic (EHD) effect using a wire-to-cylinder electrode configuration under high DC voltage. Experimental measurements demonstrated a linear relationship between the generated thrust and the corona discharge current. Furthermore, a parametric analysis revealed that increasing the electrode gap and emitter radius leads to a reduction in thrust. However, a larger electrode gap was found to enhance thrust-to-power efficiency, suggesting a trade-off between absolute thrust and system efficiency [22].

2.14 Electrohydrodynamic thrust for in-atmosphere propulsion

This study experimentally investigates electrohydrodynamic (EHD) thrust generation using wire–cylinder electrodes under high DC voltage. Recent findings highlight that

corona discharge and ionic wind can achieve a high thrust-to-power ratio, renewing interest in EHD propulsion. The paper evaluates application potential through estimates based on light aircraft parameters and thrust densities. Experimental results are presented in terms of electric field and thrust density, offering a clear overview of propulsive performance. Additionally, oscillations in airflow behind the thruster suggest wake effects, and drag variations due to collector electrode placement are analyzed, showing that aerodynamic losses can significantly affect thruster efficiency [23].

2.15 Enhanced EHD and Electrostatic Propulsion Devices Based on Polarization Effect Using Asymmetrical Metal Structure

This study reviews the development and optimization of electrohydrodynamic (EHD) and electrostatic propulsion devices, initially introduced by T.T. Brown in the 1920s. Traditional "lifters" operate with no moving parts using asymmetric electrode structures but suffer from low thrust-to-power efficiency. To address this, new models incorporating the polarization effect were proposed and tested. Experimental results showed that the improved designs generated 5.7 times more thrust than basic lifters for the same electrical input. In high-power conditions, thrust-to-power ratios approached 100 N/kW, comparable to helicopters. Numerical analyses of capacitance and charge distributions helped optimize the system's performance [24].

2.16 Electrohydrodynamic thrust for in-atmosphere propulsion

This study experimentally investigates electrohydrodynamic (EHD) thrust generation using wire–cylinder electrodes under high DC voltage. Recent findings highlight that corona discharge and ionic wind can achieve a high thrust-to-power ratio, renewing interest in EHD propulsion. The paper evaluates application potential through estimates based on light aircraft parameters and thrust densities. Experimental results are presented in terms of electric field and thrust density, offering a clear overview of

propulsive performance. Additionally, oscillations in airflow behind the thruster suggest wake effects, and drag variations due to collector electrode placement are analyzed, showing that aerodynamic losses can significantly affect thruster efficiency [23].

2.17 Experimental investigation on flow characteristics of ionic wind induced by wire electrode

This study explores ionic wind cooling technology for portable electronics using wire-wire and wire-mesh ionic wind generators with copper wire emitters. The flow characteristics of ionic wind are analyzed both qualitatively and quantitatively, showing that the square of ionic wind velocity is proportional to the applied voltage. Optimal design parameters for single-stage generators—including electrode gaps, angle, polarity, wind velocity, and efficiency—are identified. Additionally, multi-stage wire-mesh configurations demonstrate that stacking electrode pairs can increase wind velocity by up to 26.8% compared to single-stage systems, although overall efficiency remains low, limiting practical applications [25].

2.18 Force on an asymmetric capacitor

The Biefeld-Brown effect, observed when high voltage (around -30 kV) is applied to asymmetric capacitors (with electrodes of different sizes), generates a net force on the device. This force typically acts from the larger negative electrode toward the smaller positive electrode. While numerous demonstrations, such as “lifter” devices, show forces exceeding the capacitor's weight and independent of voltage polarity, the underlying mechanism remains unclear and lacks a widely accepted theory. Preliminary experiments at the U.S. Army Research Laboratory confirmed the effect’s existence. Various theoretical approaches, including ballistic ionic wind and carrier drift models, as well as thermodynamic treatments assuming nonlinear dielectric materials, have been proposed. The phenomenon holds potential for future propulsion

applications without moving parts, but further experimental and theoretical research is needed to understand and harness it fully [26].

2.19 Higher thrust-to-power with large electrode gap spacing electroaerodynamic devices for aircraft propulsion

In addition, pulse detonation engines (PDEs) are being explored as potential alternatives to traditional gas turbine engines due to their theoretically superior thermodynamic efficiency. NASA's long-term strategy also anticipates a transition toward a hydrogen-based economy, which would facilitate the development of silent, emission-free aircraft.

Electroaerodynamic (EAD) devices generate thrust in air through electrostatic acceleration and have been proposed as a propulsion method for aircraft. While theory predicts higher thrust-to-power ratios for larger electrode gaps, experimental studies beyond 100 mm gaps often show lower performance than expected. This discrepancy is explained by three effects: leakage current to surroundings, which increases power consumption without producing thrust; reverse corona emission reducing thrust and increasing power; and the thruster's electric potential relative to its environment affecting both factors. Experiments with gap spacings between 50 and 300 mm confirm that when these effects are considered, classical EAD theory remains valid. Numerical simulations support the experimental findings with close accuracy. The study achieved thrust-to-power ratios up to 15 N/kW for large gap thrusters, two to three times better than smaller gap devices, demonstrating promise for future EAD propulsion systems competitive with conventional methods [27].

2.20 Investigations on Thrust-to-power of an ionic wind propulsion

The Biefeld-Brown effect, discovered in the 1920s, describes thrust generation via ionic wind created by a pair of asymmetrical high-voltage electrodes. This phenomenon offers an alternative to conventional aircraft propulsion with benefits

such as no moving parts, quiet operation, and zero combustion emissions. In 2018, MIT demonstrated the first solid-state propulsion airplane powered by ionic wind, achieving steady flights lasting around 10 seconds with a 5 m wingspan. Experimental studies on electroaerodynamic (EAD) thrusters with electrode gaps up to 80 mm reported a maximum thrust of 220 mN/m and a thrust-to-power ratio of 8.9 N/kW at 100 mN/m thrust. Future work focuses on improving the thrust-to-power efficiency for practical EAD airplane applications [28].

2.21 Review on the history, research, and applications of electrohydrodynamics

Corona discharge occurs when the electric field near a conductor ionizes the surrounding dielectric without causing electrical breakdown. Although generally undesirable in high-voltage systems, controlled corona discharge is utilized to ionize fluids and generate motion by converting electrical energy into kinetic energy—a process known as electrohydrodynamic (EHD). This review summarizes research on EHD effects related to corona discharge, covering early observations, recent mathematical models, and practical applications including thrust generation, heat transfer enhancement, boundary layer control, drying, fluid pumping, and cooling [29].

2.22 Successively accelerated ionic wind with integrated dielectric-barrier-discharge plasma actuator for low-voltage operation

Electrohydrodynamic (EHD) force enables active fluid flow control and thrust generation through ionic wind without moving parts. This study proposes a method to generate unidirectional ionic wind using a surface Dielectric-Barrier-Discharge (DBD) plasma actuator with multiple electrodes. Unlike conventional methods that produce opposing ionic winds, the new design of voltage waveforms and electrode arrangements successfully creates a strong, unidirectional EHD force by controlling dielectric surface charge. This approach allows strong ionic wind generation without

requiring bulky high-voltage power supplies, making it promising for enhancing aerodynamic performance in small unmanned aerial vehicles [30].

2.23 Propulsion and power for 21st century aviation

Future air transportation demands revolutionary advancements to ensure increased safety, reliability, environmental sustainability, and affordability. In alignment with these objectives, NASA envisions the development of next-generation propulsion systems that are highly efficient, intelligent, nearly silent beyond airport boundaries, and produce near-zero emissions of harmful pollutants such as CO_2 and NO_x. A key element of this vision includes adaptive intelligent engines capable of autonomously responding to dynamic internal and external conditions to optimize performance with minimal or no human intervention. One of the most transformative concepts under investigation is distributed vectored propulsion, which aims to replace conventional two- to four-engine wing- or fuselage-mounted configurations with arrays of small, mini, or micro engines, offering enhanced control and efficiency [31].

2.24 A novel unmanned aircraft with solid-state control surfaces: Analysis and flight demonstration

The study concludes that to improve the propulsive efficiency of corona discharge systems, future research should focus on strategies to reduce the effective ion mobility, thereby enhancing energy transfer from electric fields to useful thrust. This work establishes a theoretical and empirical baseline for the continued development of electrohydrodynamic (EHD) propulsion technologies.

In 2010, the Virginia Tech Wing Morphing Design Team developed a fully servo-less, solid-state piezoelectric control system for a remotely piloted fixed-wing aircraft, marking a significant milestone in morphing aircraft technology. The aircraft, designed as part of a senior project between the Departments of Mechanical Engineering and Aerospace and Ocean Engineering, utilized Macro-Fiber Composite

(MFC) piezocomposite actuators to dynamically alter the camber of all control surfaces, eliminating the need for traditional servomechanisms. Aerodynamic performance was theoretically analyzed using vortex lattice methods to inform the design of the control surfaces and predict control response. These analyses were supported by wind tunnel experiments, which measured steady-state roll rates and compared them with a similarly sized aircraft using conventional servo-actuated surfaces. The results demonstrated sufficient stability and control authority, validating the design approach. On April 29, 2010, the aircraft achieved its first successful flight, becoming the first fully MFC-controlled, untethered, flight-tested fixed-wing aircraft. Powered by an electric motor and a single lithium polymer battery, the vehicle serves as a pioneering example of solid-state maneuvering technology in small-scale aviation [32].

2.25 Design and implementation of a lightweight high-voltage power converter for electro-aerodynamic propulsion

The growing interest in electro-aerodynamic (EAD) propulsion systems has underscored the need for lightweight high-voltage power converters capable of delivering tens of kilovolts at power levels of several hundred watts. In response to this demand, recent work[33] has demonstrated a converter design that operates from a 160–200 V DC input and delivers up to 600 W at 40 kV, with a switching frequency of approximately 500 kHz and a specific power of 1.2 kW/kg. This performance represents a significant improvement over conventional industrial and academic converters in terms of power-to-weight ratio at comparable output levels. The converter architecture comprises three primary stages: an inverter, a step-up transformer, and a high-voltage rectifier, each contributing to the overall voltage gain. The study systematically compares various design approaches for these stages, emphasizing weight minimization through optimal distribution of voltage gain and careful component selection, all within the constraints of device limitations and thermal/electrical losses.

2.26 Enhancement of external forced convection by ionic wind

Ionic wind, generated by ion-neutral collisions in an electric field, offers a promising approach for enhancing convective heat transfer without moving parts. In a study [34] utilizing a corona discharge between a steel wire and copper tape electrodes on a flat plate, significant improvements in heat transfer were observed. The discharge, aligned with bulk flow, increased local heat transfer coefficients by over 200%. Infrared imaging confirmed uniform cooling along the wire, and both experimental and analytical results showed the heat transfer coefficient scales with the fourth root of the corona current. Additionally, electrode spacing influenced the area, but not the peak, of heat transfer enhancement. These findings highlight the purely hydrodynamic nature of the cooling effect.

2.27 A review on recent advances and challenges of ionic wind produced by corona discharges with practical applications

Ionic wind, produced during corona discharge, offers silent operation and requires no moving parts, making it attractive for various applications. However, its generation involves complex processes including gas ionization, recombination, and chemical interactions. Understanding these mechanisms is essential for advancing practical applications. Recent reviews present the fundamentals of corona discharge and ionic wind generation, alongside developments in generator design based on experiments and simulations. Key challenges—such as high onset voltage, ozone emission, and sensitivity to environmental conditions—remain obstacles to real-world use. Research continues to explore mitigation strategies and future directions for effective integration of this technology [35].

2.28 The characteristics of ionic wind and its effect on electrostatic precipitators

Ionic wind significantly influences the flow field and performance of electrostatic precipitators (ESPs), particularly at low velocities. Numerical simulations using 2D and 3D turbulence models and the SIMPLE-C scheme were employed to analyze this effect. Results show that while the impact of ionic wind is minimal under normal conditions, it becomes substantial when the flow velocity drops below 0.6 m/s, reducing collection efficiency and increasing turbulence. At velocities below 0.23 m/s, the collection efficiency may drop by approximately 12%, highlighting the need to account for ionic wind effects in low-flow ESP designs [36].

2.29 A dielectric barrier discharge ion source increases thrust and efficiency of electroaerodynamic propulsion

Electroaerodynamic (EAD) propulsion offers a solid-state, nearly silent alternative for electric aircraft, eliminating combustion emissions. While conventional EAD thrusters use DC corona discharges for ion generation and acceleration, they suffer from a thrust-efficiency trade-off, limiting their practicality. Recent advancements propose using dielectric barrier discharge (DBD) for ion production while maintaining a DC acceleration field, achieving significantly higher thrust-to-power ratios—up to 20 N/kW at 50 mN/m and 10 N/kW at 150 mN/m—doubling the performance of corona-based systems. This improvement suggests DBD-enhanced EAD could enable more efficient and practical solid-state aircraft [37].

CHAPTER 3

METHOD/EXPERIMENTAL

To investigate the proposed concepts, a series of experiments were designed and conducted. This section outlines the experimental procedures, apparatus, and measurement techniques used to validate the existence of ionic wind, quantify the produced thrust, and evaluate the actuator's mechanical performance. The methodology is structured to progressively build upon each step—starting from the visualization of ionic wind, followed by thrust characterization, and culminating in dynamic testing of the actuator system.

3.1 Ionic wind demonstration using appropriate setup

Ionic wind generated by experimental setup was prepared at the Electronic Nose Laboratory of the Faculty of Aeronautics and Astronautics at University of Turkish Aeronautical Association. DEVMO-DC 3V-6V-400kV Power Module-High Voltage Generator was used for reaching the required voltage level, generator is shown in Figure 3.1. An example circuit diagram from another study [4] is shown in Figure 3.2. Electrodes consist of two circular conductive parts. Smoke and candles were utilized as visualization methods, with the candle being preferred due to its ease of observation and interpretation. The schematic diagram of high voltage generator is shown in Figure 3.3. And measurements using a Pitot tube were attempted. The schematic diagram of this study is shown in Figure 3.4.

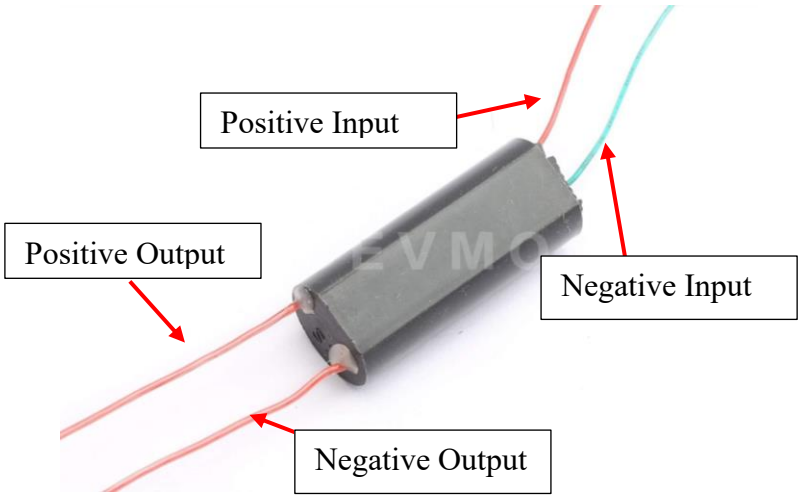

Figure 3.1 DEVMO-DC 3V-6V-400kV Power Module-High Voltage Generator used to generate plasma

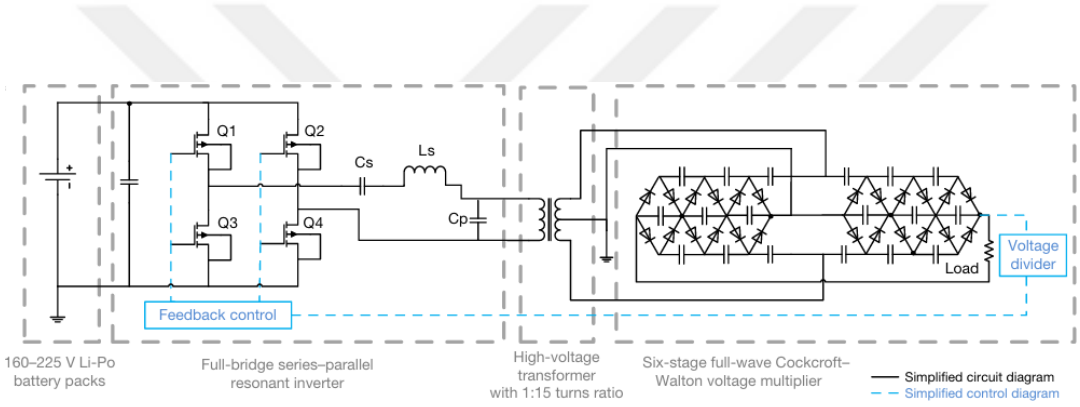

Figure 3.2 The high-voltage power converter (HVPC) comprises three stages: a series–parallel resonant inverter converting 160–225 V DC to high-frequency AC, followed by a high-voltage transformer that steps up the AC voltage.

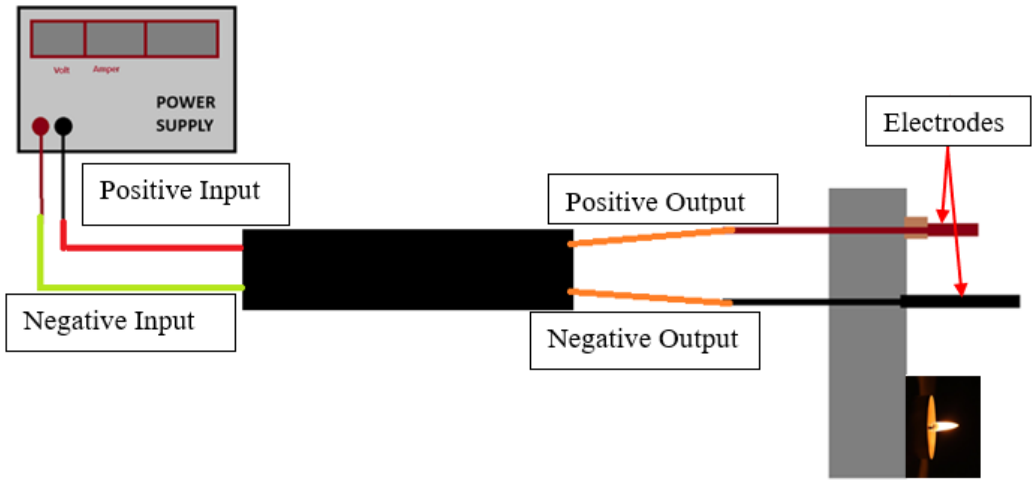

Figure 3.3 Schematic of an ionic wind demonstration by candle test set-up

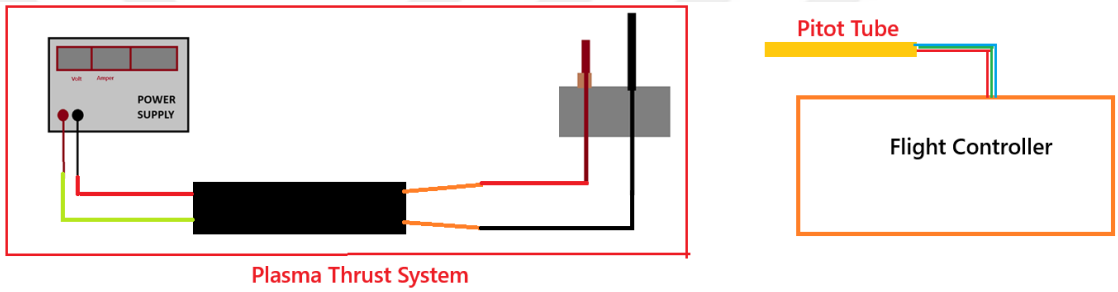

Figure 3.4 Schematic of Air Speed Measurement System by Pitot Tube

3.2 Thrust measurement

The ionic wind phenomenon is governed by the equations presented in (3.1), which illustrates the variables influencing its behavior. A representative graph adapted from [17] is provided in Figure 2.1 to demonstrate the relationship among the relevant parameters.

$$T = \frac{Id}{\mu} \tag{3.1}$$

Where T is thrust, d is electrode distance, and μ is ionic mobility.

The distance between the electrodes and the output current directly affects the thrust value. For this reason, the thrust test setup was performed by increasing the power amount according to the distances for 3 different distances (12, 15, and 20 mm). When the formula is examined, it is expected that thrust and power will move linearly. The distance between them can be adjusted to alternate between 12mm, 15mm and 20mm. Our objective in analyzing various electrode distances is to determine the optimal distance and incorporate it into our design while maintaining it as a constant parameter. A positive voltage is applied to the part with a smaller radius, while a negative charge is applied to the emitter electrode with a larger radius. This system is then placed on a sensitive laboratory scale along the vertical axis. The thrust values obtained at varying electrical power levels are recorded to create a data set. From these measurements, the thrust-to-power ratio is calculated using Equation (3.2).

$$\Theta = \frac{T}{P} \tag{3.2}$$

Where Θ is thrust-to-power ratio, T is thrust, and P is electrical input power.

Additionally, the thrust density is calculated using Equation (3.3).

$$ø = \frac{T}{A} \tag{3.3}$$

Where ø is thrust density, T is thrust, and A is electrode area.

For each electrode distance, measurements are taken twice. The results will be displayed as points on a graph and their linearity will be shown. The test set up is shown in Figure 3.5. The schematic diagram of test set up is shown in Figure 3.6.

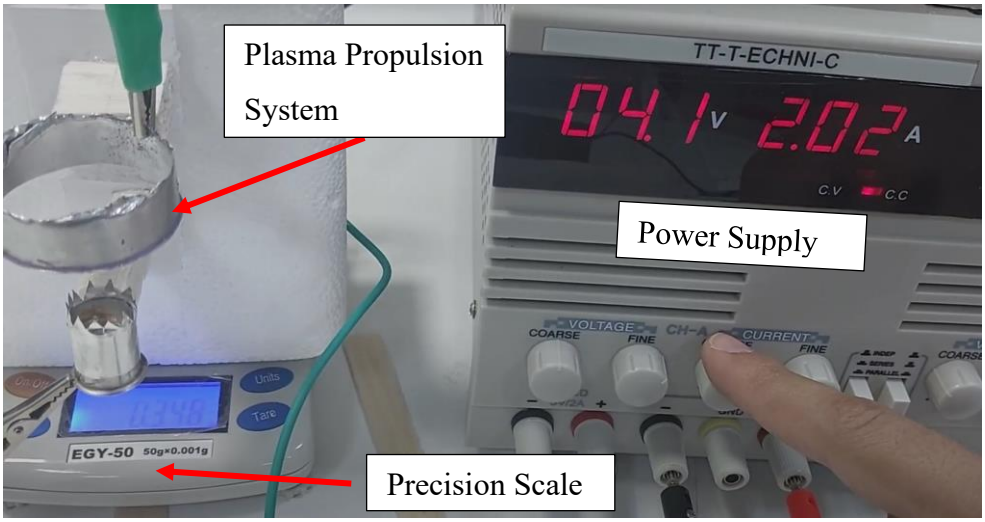

Figure 3.5 Sample Thrust Measurement System

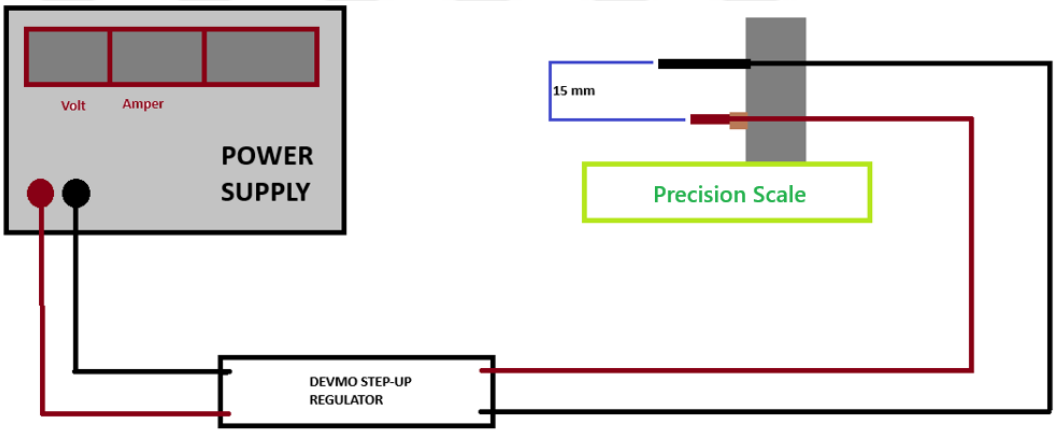

Figure 3.6 Schematic of Thrust Measurement System

3.3 Demonstrated mechanical action

Following the necessary tests, speed tests are conducted in the optimum electrode distance configuration. For these tests, a plasma thruster is installed on each end of a 1-meter-long rod at an optimum electrode distance and data is recorded based on varying electrical voltage and current levels. In this way, the optimum voltage and current value will be calculated.

Upon data collection speed values are analyzed and the efficiency value will be calculated by (3.4).

$$\eta = \frac{P_{output}}{P_{input}} = \frac{T\ v}{P} \tag{3.4}$$

Where T is thrust, v is speed, and P is input electrical power.

The two different measurement systems prepared are shown in Figure 3.7 and Figure 3.9. The test set up schemas are shown in Figure 3.8 and Figure 3.10 .Experimental setup number one is powered by an external power source, and electricity is supplied to the rotating system via a bearing. The purpose of this test is to find the optimum voltage and current values at which the system operates. Experimental setup number two is powered by a battery (Leopard Power 4200mAh 11.1V 3s 40C LiPo Battery) and power modules mounted on the rod, supplying energy to the power modules. Due to the weight of the battery and modules, the mass of system number two is 852 grams, while system number one is 520 grams.

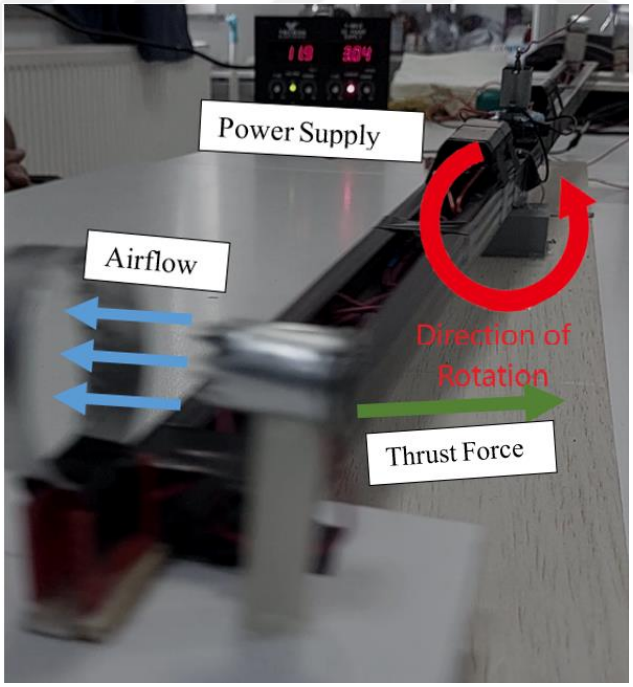

Figure 3.7 Sample power-supplied speed measurement system (Experiment Setup1)

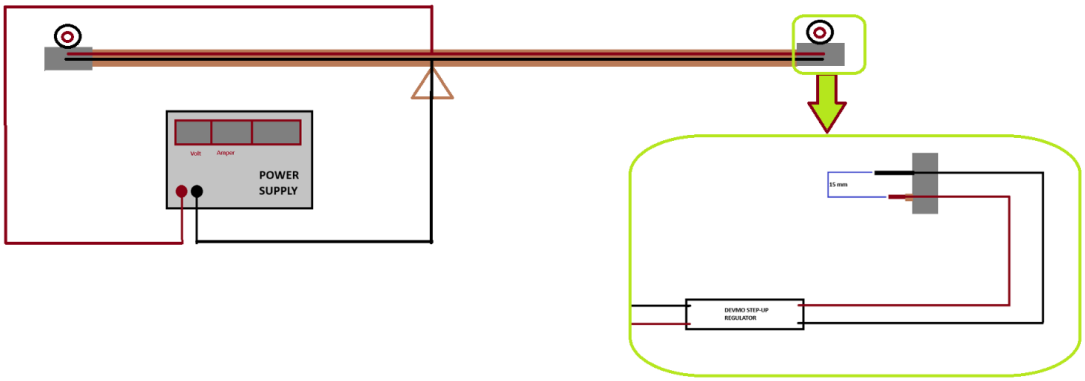

Figure 3.8 Power-supplied speed measurement system schematic (Experiment Setup1)

Figure 3.9 Sample battery-powered speed measurement system (Experiment Setup2)

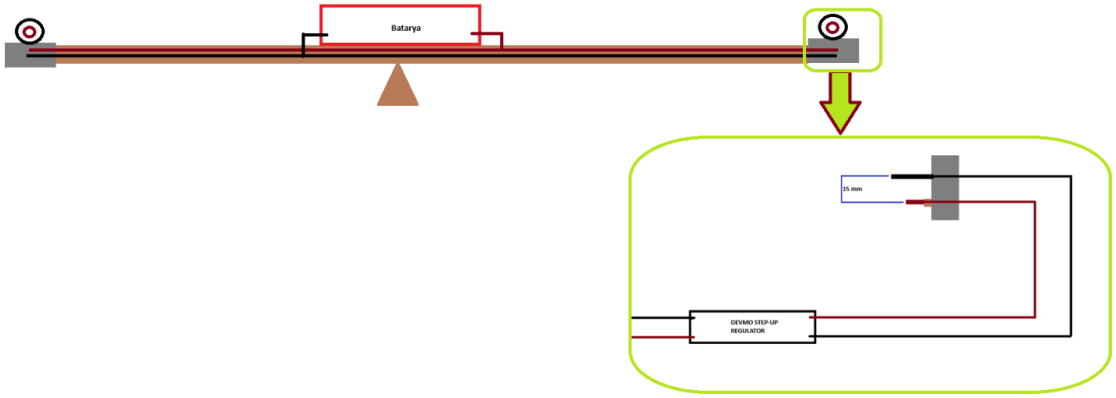

Figure 3.10 Battery-powered speed measurement system schematic (Experiment Setup 2)

CHAPTER 4

RESULTS

4.1 Ionic wind demonstration using appropriate setup

The airflow generated by the system was observed using a candle, as illustrated in Figure 4.1. These figures demonstrate that the system can generate airflow.

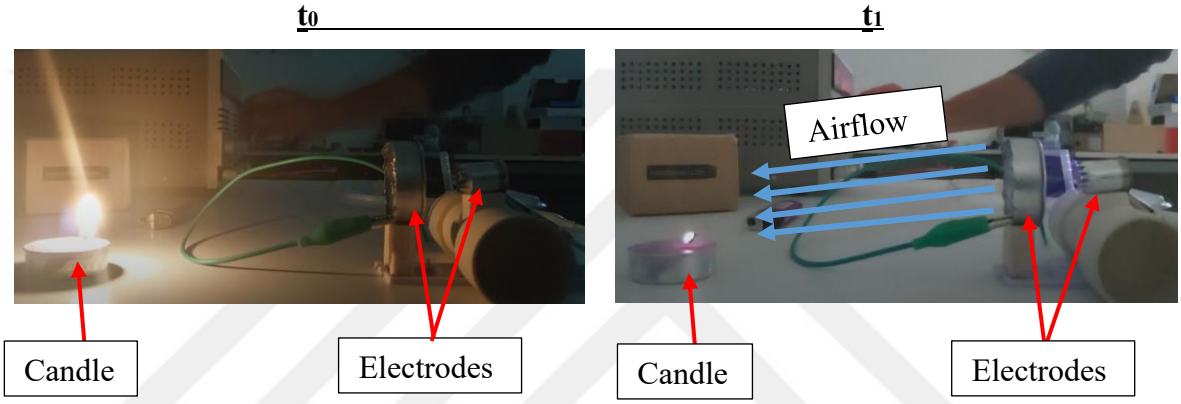

Figure 4.1 At time t_0, system is not operating, while at time t_1, power is supplied to the system, and airflow is observed.

Initial attempts to measure the airspeed using a Pitot tube, results are approximately 2.50 m/s but these were inaccurate. The data extracted using the code presented in Appendix B was plotted in Table 4.1. As illustrated in the table, the dataset exhibits significant instability. Consequently, the Pitot tube proved unsuitable for reliable measurements at the low speeds encountered in this study.

Table 4.1 Graph Pitot Tube Test Data Result

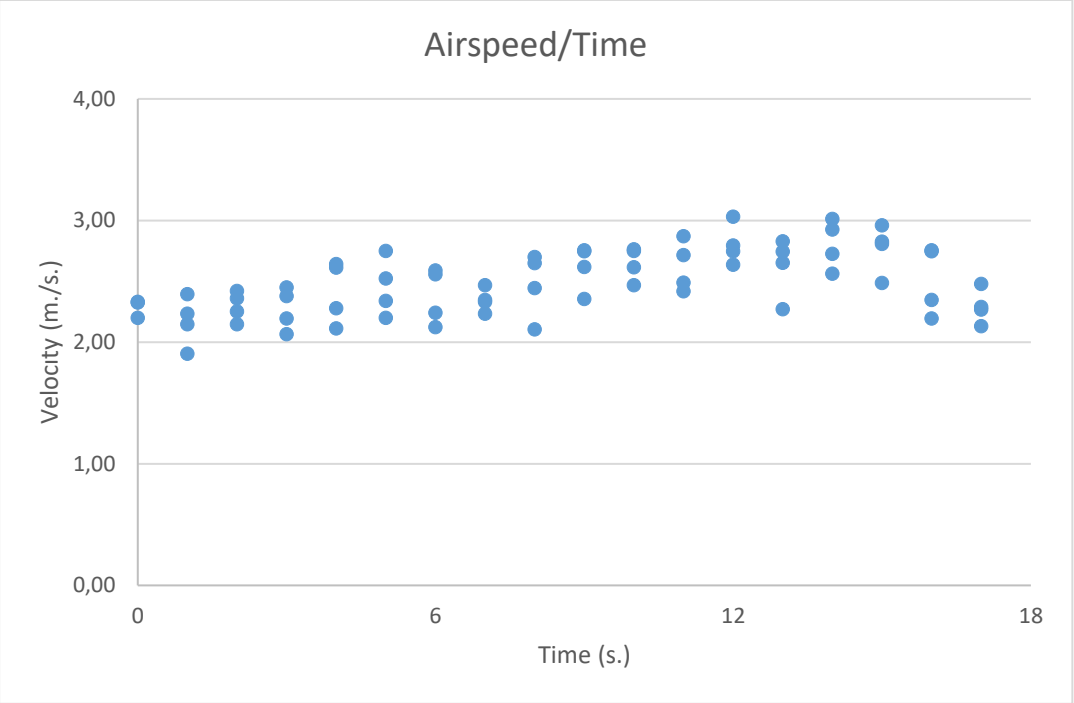

4.2 Thrust measurement

In the thrust to power graphs, the y-axis represents thrust in grams, while the x-axis represents the power delivered to the step-up regulator in watts. The test graphs and data shown in Figure 4.2 present the results for 12 mm, 15 mm, and 20 mm distances. Detailed data information is in Appendix C. Data points are linearized and shown in graphs, thus revealing the linearity of the thrust and applied power.

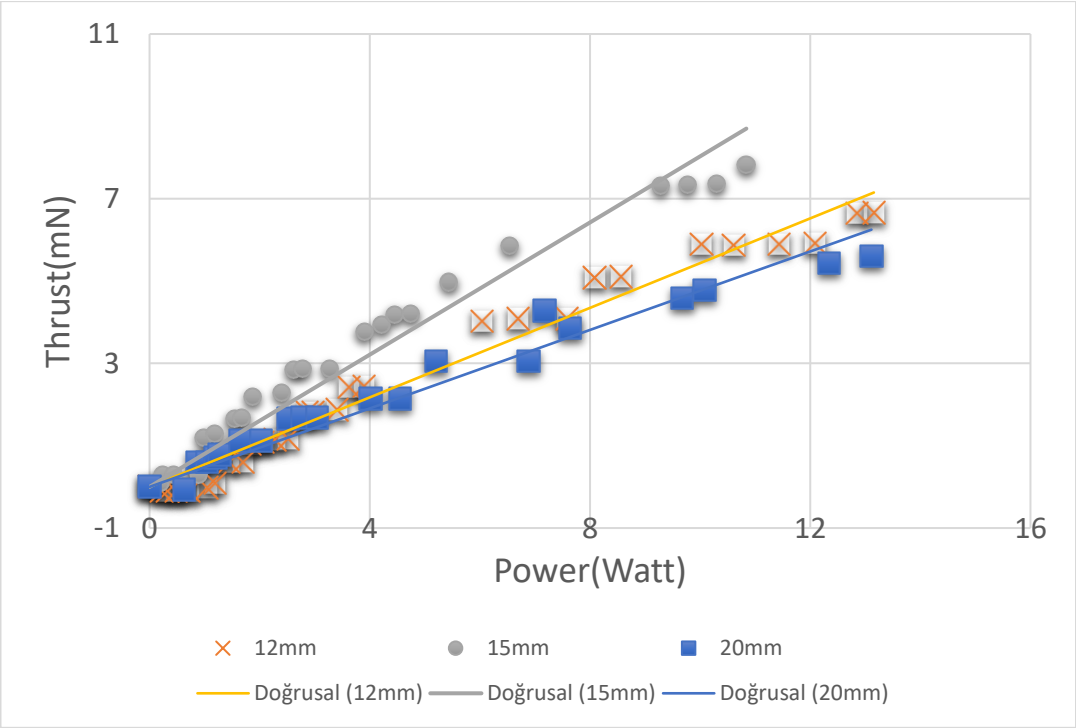

Figure 4.2 The experimental thrust to power graph conducted for 12, 15 mm, and 20 mm electrode distance

When the results are examined, the highest thrust at equal power value is reached at 15mm. The thrust power ratio of this value is as follows:

$$\Theta = \frac{T}{P} = 0.72 \frac{N}{kW} \tag{4.1}$$

Collector electrode radius is 19 mm. When the results are examined, the highest thrust at equal power value is reached at 15mm. The thrust density of this value is as follows:

$$ø = \frac{T}{A} = 6.89 \frac{N}{m^2} \tag{4.2}$$

For this reason, in the next studies, the experimental setups will be designed according to 15 mm. Current / Power graphs present input voltage and discharge current values

for 12 mm, 15 mm, and 20 mm tests in Figure 4.3. And, output voltage and discharge current values for 12 mm, 15 mm, and 20 mm tests in Figure 4.4. And current values are calculated by using (3.1), efficiency of regulator is assumed 1. Due to the unavailability of direct current measurements, the current value was estimated based on Equation (3.1). And μ value is taken as 2.1×10^{-4} $m^2/V\cdot s$ [17]. Voltage values were calculated according to power conservation. Due to the unavailability of direct voltage measurements. Data points are linearized and shown in graphs, thus revealing the linearity of the current and applied power.

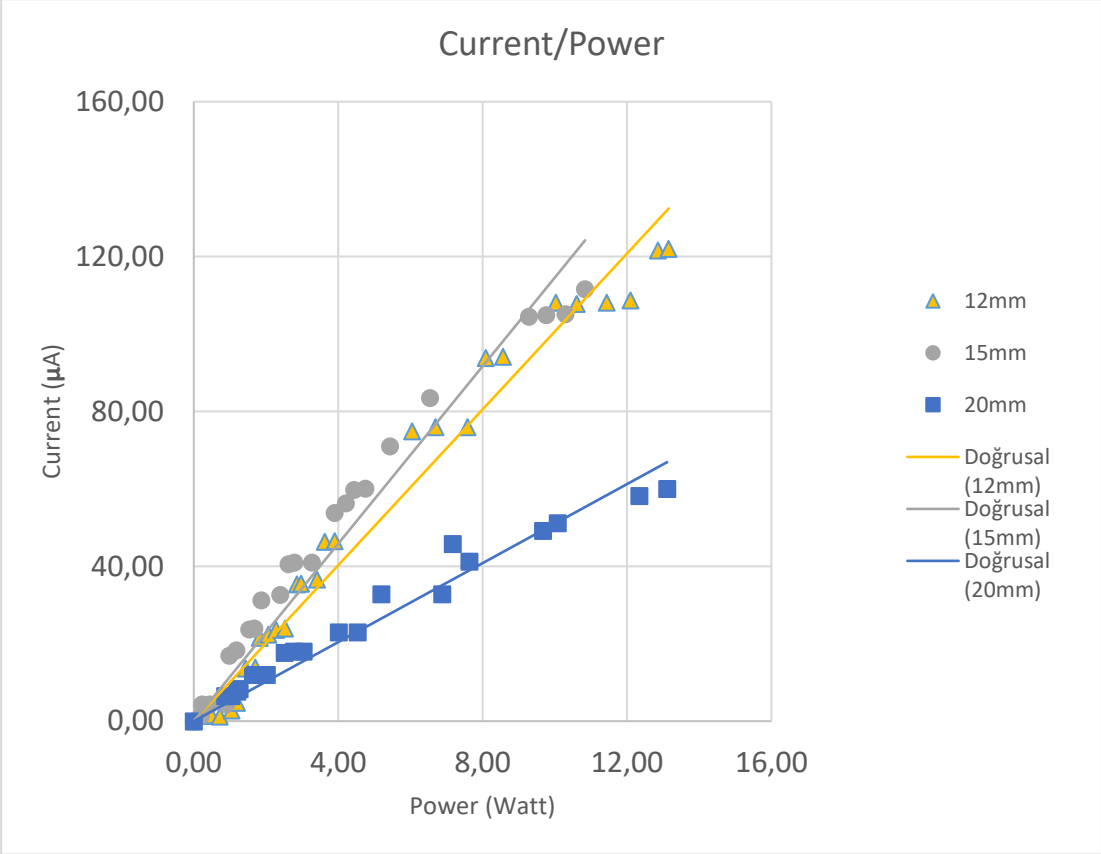

Figure 4.3 The Discharge Current/Power graph conducted for 12 mm, 15 mm, and 20 mm electrode distance

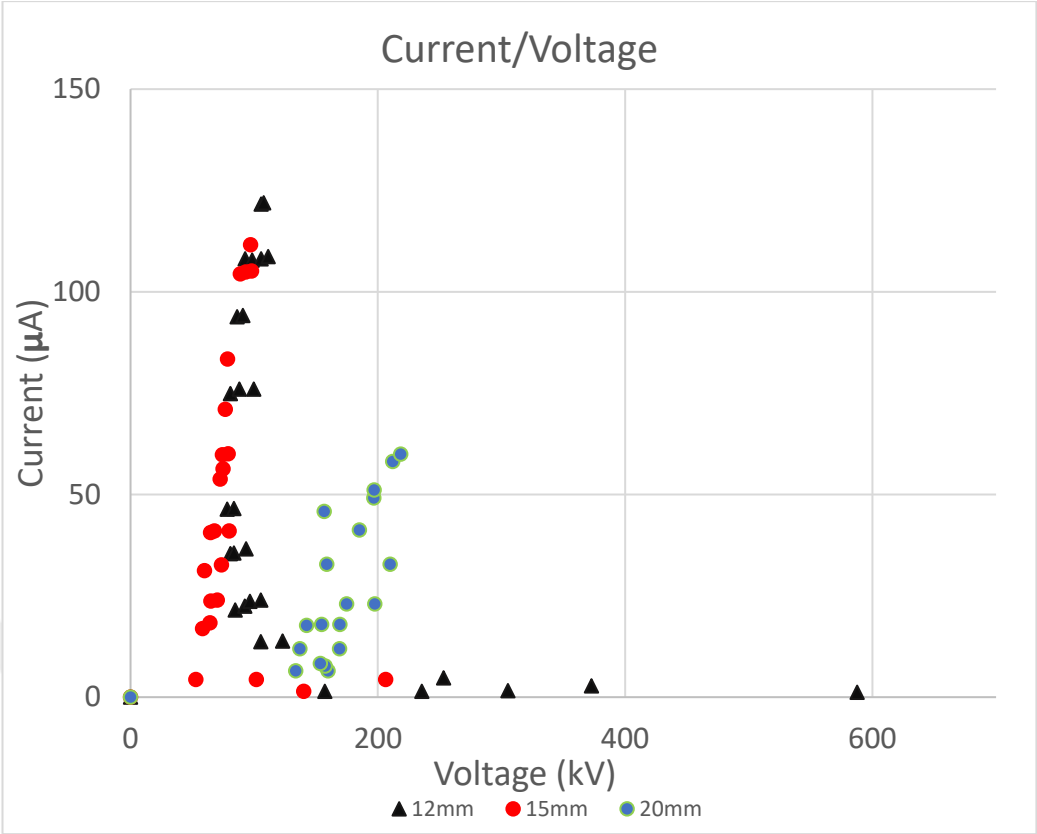

Figure 4.4 The Discharge Current/Voltage graph conducted for 12 mm,15 mm, and 20 mm electrode distance

4.3 Demonstrated mechanical action

Instead of this measurement method plasma thruster is installed on each end of a 1-meter-long rod at an optimum electrode distance fixed at the optimum value of 15 mm. The test results for speed are presented in Table 4.2. In the first experiment, no motion was observed in the system prepared with experimental setup 1, which was supplied with 23.40 Watts. In the second experiment prepared with Experimental Setup 1, supplied with 34.51 Watts. In the third experiment the system prepared with Experimental Setup 1, which was supplied with 49.35 Watts. In the fourth experiment the system prepared with Experimental Setup 1, which was supplied with 68.88 Watts. The data indicates that operating the regulator outside its optimal range results in noticeable inefficiencies. Maintaining a current of approximately 3 A while ensuring

the voltage does not exceed 6 V per regulator leads to optimal performance. In the last experiment, the system was prepared with Experimental Setup 2, which was supplied with 31.80 Watts. The Experimental Setup 1 and Experimental Setup 2 speed graph is shown in Figure 4.5.

Table 4.2 The Electrical Power Values Applied to Test Systems 1 and 2

Power (Watt)	Voltage (Volt)	Current (Amper)	System
23.40	10.00	2.34	Experimental Setup 1
34.51	11.90	2.90	Experimental Setup 1
49.35	14.10	3.50	Experimental Setup 1
68.88	16.80	4.10	Experimental Setup 1
31.80	5.30	6.00	Experimental Setup 2

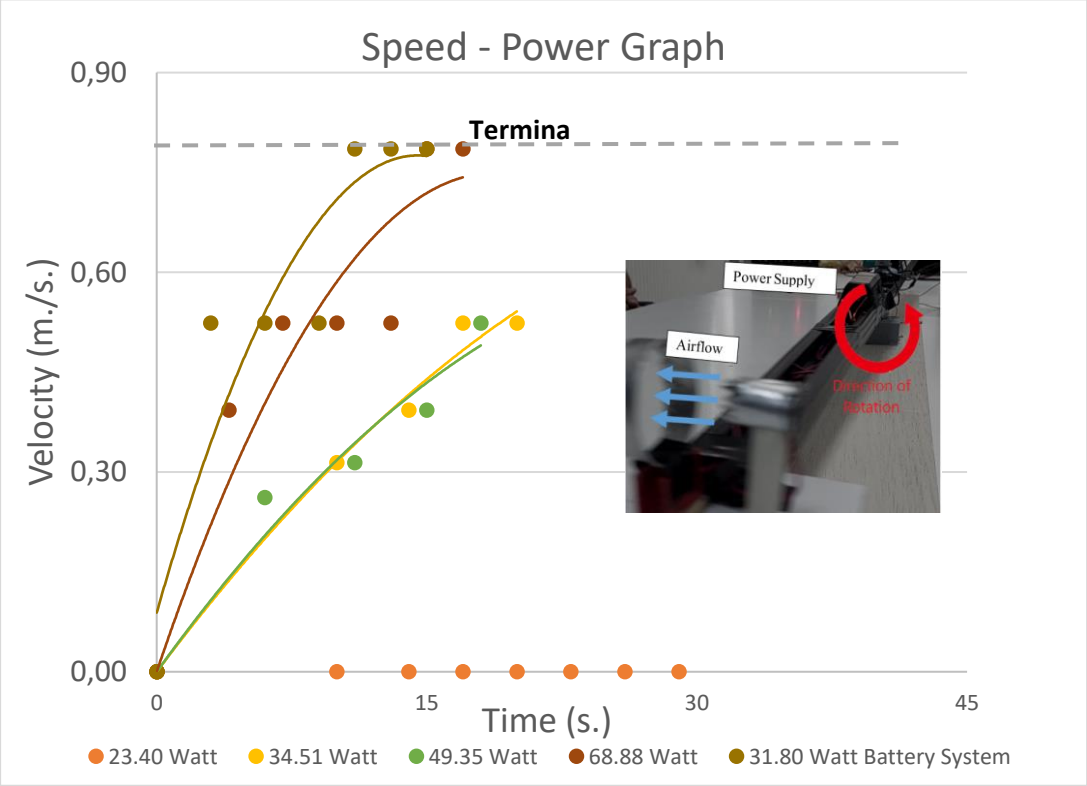

Figure 4.5 All speed graphs of Experimental Setup 1 and Experimental Setup 2

When the graphs obtained from the thrust measurement tests are examined, it has been observed that the thrust generally increases linearly with increasing power values.

Apart from the second experiment with the battery system, inefficiency is noticeable as the optimum voltage value is deviated from. As a result of the speed tests, the highest speed was achieved in the second experiment. The results of the second experiment are as follows: a speed of 0.79 m/s which is also our terminal speed. Efficiency and thrust to power ratio calculation are shown below. Power efficiency is calculated as 0.04%.

Table 4.3 Masses of Components in the Second Analysis Setup

Geometry	**Mass**				
Collector r	**Battery**	**Power Module**	**Regulator**	**Rod**	**Total**
19	0.33	0.07	0.10	0.35	0.85
mm	kg	kg	kg	kg	kg

$$\eta = \frac{\mathrm{P_{output}}}{P_{input}} = \frac{0.01\ \mathrm{Watt}}{31.80\ Watt} = 0.04\% \tag{4.3}$$

CHAPTER 5

CONCLUSION

The generation of ionic wind was successfully demonstrated with the aid of a candle and a pitot tube. Despite the presence of considerable inaccuracy, the air speed was measured to be approximately 2.50 m/s. Following this observation, thrust testing was initiated. The thrust tests conducted demonstrate that thrust and power values are generally linear. The optimal electrode distance is 15mm. The thrust value obtained at this electrode distance is 7.82 mN. The calculated results consistent with this value are as follows: ø = 6.89 N/m² and Θ = 0.72 N/kW. When compared with previous studies, particularly the one conducted at [4], notable differences were observed. In that study, these values were obtained: ø = 3 N/m² and Θ = 6.25 N/kW. In speed tests, it was also determined that speed is linear with power. However, the highest value was measured as 0.79 m/s in Experiment 2 by less power, as the optimal voltage and current range were exceeded in tests other than the setup with Battery. The efficiency of this system is 0.04%. The importance of selecting a suitable high-voltage generator and providing the correct voltage for the systems to be designed have been understood. The current results have proven that the thrust required for the necessary maneuvers is generated by our system. Compared to conventional aircraft, our study, which will feature fewer components for control surfaces, not only offers structural simplicity and elegance but also advantages such as ease of maintenance and noiselessness. The complexity of an example conventional control surface is shown in Figure 1.1. The solid-state maneuvering system is highly suitable for High-Altitude Pseudo-Satellite (HAPS) platforms due to structural simplicity and elegance and capability for thrust distribution. However, the efficiency value and thrust power ratio are quite low. Therefore, it was not possible to integrate and demonstrate this system on an actual aircraft.

REFERENCES

[1] Wilson, J., Perkins, H. D., & Thompson, W. K. (2009). An Investigation of Ionic Wind Propulsion. NASA/TM-2009-215822.

[2] Anderson Jr., J. D. (2014). Control and Stability. In J. D. Anderson Jr. (Ed.), Introduction to Flight (8th ed., pp. 594-653). McGraw-Hill Education.

[3] Raymer, D. P. Aircraft Design: A Conceptual Approach, 4th ed. American Institute of Aeronautics and Astronautics, Reston, VA, 2006.

[4] Xu, H., He, Y., Strobel, K. L., Gilmore, C. K., Kelley, S. P., Hennick, C. C., Schierl, T., Woolston, M., Perreault, D. J., & Barrett, S. R. H. (2018b). Flight of an aeroplane with solid-state propulsion. Nature, 563(7732), 532–535.

[5] Goldstein, H., Poole, C. P., & Safko, J. L. (2002). Classical mechanics (3rd ed.). Addison-Wesley.

[6] Monrolin, N., Praud, O., & Plouraboué, F. (2018). Electrohydrodynamic ionic wind, force field, and ionic mobility in a positive dc wire-to-cylinders corona discharge in air. Physical Review Fluids, 3(6), 063701.

[7] Göksel, B., Fischer, M., Rechenberg, I., & Thallemer, A. (2005). Elektrostatischer Plasma-Wellantrieb für Bionische Luftschiffe. In Proceedings of the German Aerospace Congress (pp. 1853-1856).

[8] Nadar, R. (2023). Futuristic Exploring of Ionic Wind Technology and Wind-Assisted Propulsion in a Comprehensive Journey. Acceleron Aerospace Journal, 1(6), 121-125.

[9] Colas, D. F., Ferret, A., Pai, D. Z., Lacoste, D. A., & Laux, C. O. (2010). Ionic wind generation by a wire-cylinder-plate corona discharge in air at atmospheric pressure. Journal of applied physics, 108(10).

[10] Chung, J. H., Sohn, D. K., & Ko, H. S. (2023). Study on the Influence of Central Hole Diameter in a Wire Mesh Electrode on Ionic Wind Characteristics. Micromachines, 14(8), 1614.

[11] Rickard, M., Dunn-Rankin, D., Weinberg, F., & Carleton, F. (2005). Characterization of ionic wind velocity. Journal of Electrostatics, 63(6-10), 711-716.

[12] Gilmore, C. K., & Barrett, S. R. (2015). Electrohydrodynamic thrust density using positive corona-induced ionic winds for in-atmosphere propulsion. Proceedings of the Royal Society A: Mathematical, Physical and Engineering Sciences, 471(2175), 20140912.

[13] De Wit, A. J., Lammen, W. F., Vankan, W. J., Timmermans, H., Van Der Laan, T., & Ciampa, P. D. (2020). Aircraft rudder optimization-A multi-level and knowledge-enabled approach. Progress in Aerospace Sciences, 119, 100650.
[14] Gaur, D., & Tengli, P. N. Structural Analysis and Optimization of Aircraft Rudder.
[15] Gheorghe, A., Zolghadri, A., Cieslak, J., Goupil, P., Dayre, R., & Le Berre, H. (2013). Model-based approaches for fast and robust fault detection in an aircraft control surface servo loop: From theory to flight tests [applications of control]. IEEE Control Systems Magazine, 33(3), 20-84.
[16] Christenson, E.A., and Moller, P.S., "Ion-Neutral Propulsion in Atmospheric Media," AIAA Journal, vol. 5, no. 10, pp. 1768–1773, (1967).
[17] Sigmond, R.S., "Simple approximate treatment of unipolar space-charge-dominated coronas: The Warburg law and the saturation current," Journal of Applied Physics, vol. 53(2), February 1982, pp. 891–898.
[18] Zheng, P., Wu, J., Zhang, Y., & Wu, B. (2020). A Comprehensive Review of Atmosphere-Breathing Electric Propulsion Systems. International Journal of Aerospace Engineering, 2020(1), 8811847.
[19] Li, L., Lee, S. J., Kim, W., & Kim, D. (2015). An empirical model for ionic wind generation by a needle-to-cylinder dc corona discharge. Journal of Electrostatics, 73, 125-130.
[20] Shimizu, K., Mizuno, Y., & Blajan, M. (2015). Basic study on flow control by using plasma actuator. IEEE Transactions on Industry Applications, 51(4), 3472-3478.
[21] Guerra-Garcia, C., Nguyen, N. C., Mouratidis, T., & Martinez-Sanchez, M. (2020). Corona discharge in wind for electrically isolated electrodes. Journal of Geophysical Research: Atmospheres, 125(16), e2020JD032908.
[22] Kiousis, K. N., Moronis, A. X., & Fruh, W. G. (2014). Electro-hydrodynamic (EHD) thrust analysis in wire-cylinder electrode arrangement. Plasma Science and Technology, 16(4), 363.
[23] Monrolin, N., Plouraboué, F., & Praud, O. (2017). Electrohydrodynamic thrust for in-atmosphere propulsion. AIAA Journal, 55(12), 4296-4305.
[24] Saiki, T. (2015). Enhanced EHD and Electrostatic Propulsion Devices Based on Polarization Effect Using Asymmetrical Metal Structure. Journal of Electrical and Electronic Engineering, 3(4), 76-86.
[25] Feng, J., Wang, C., Wu, C., & Liu, Q. (2021). Experimental investigation on flow characteristics of ionic wind induced by wire electrode. Journal of the Chinese Institute of Engineers, 44(1), 22-32.
[26] Bahder, T. B., & Fazi, C. (2002). Force on an asymmetric capacitor. arXiv preprint physics/0211001.

[27] Xu, H., Gomez-Vega, N., Agrawal, D. R., & Barrett, S. R. (2019). Higher thrust-to-power with large electrode gap spacing electroaerodynamic devices for aircraft propulsion. Journal of Physics D: Applied Physics, 53(2), 025202.
[28] Schichler, U. (2020, September). Investigations on Thrust-to-power of an ionic wind propulsion. In 2020 IEEE International Conference on High Voltage Engineering and Application (ICHVE) (pp. 1-4). IEEE.
[29] Fylladitakis, E. D., Theodoridis, M. P., & Moronis, A. X. (2014). Review on the history, research, and applications of electrohydrodynamics. IEEE Transactions on Plasma Science, 42(2), 358-375.
[30] Sato, S., Furukawa, H., Komuro, A., Takahashi, M., & Ohnishi, N. (2019). Successively accelerated ionic wind with integrated dielectric-barrier-discharge plasma actuator for low-voltage operation. Scientific reports, 9(1), 5813.
[31] Sehra, A. K., & Whitlow Jr, W. (2004). Propulsion and power for 21st century aviation. Progress in aerospace sciences, 40(4-5), 199-235.
[32] Bilgen, O., Butt, L. M., Day, S. R., Sossi, C. A., Weaver, J. P., Wolek, A., ... & Inman, D. J. (2013). A novel unmanned aircraft with solid-state control surfaces: Analysis and flight demonstration. Journal of Intelligent Material Systems and Structures, 24(2), 147-167.
[33] He, Y., Woolston, M. R. & Perreault, D. J. Design and implementation of a lightweight high-voltage power converter for electro-aerodynamic propulsion. In IEEE Workshop on Control and Modeling for Power Electronics http://doi. org/10.1109/COMPEL.2017.8013315 (IEEE, 2017).
[34] Go, D. B., Maturana, R. A., Fisher, T. S., & Garimella, S. V. (2008). Enhancement of external forced convection by ionic wind. International Journal of Heat and Mass Transfer, 51(25-26), 6047-6053.
[35] Qu, J., Zeng, M., Zhang, D., Yang, D., Wu, X., Ren, Q., & Zhang, J. (2021). A review on recent advances and challenges of ionic wind produced by corona discharges with practical applications. Journal of Physics D: Applied Physics, 55(15), 153002.
[36] Liang, W. J., & Lin, T. H. (1994). The characteristics of ionic wind and its effect on electrostatic precipitators. Aerosol Science and Technology, 20(4), 330-344.
[37] Xu, H., He, Y., & Barrett, S. R. (2019). A dielectric barrier discharge ion source increases thrust and efficiency of electroaerodynamic propulsion. Applied Physics Letters, 114(25).
[38] Chattock, A. P. (1899). XLIV. On the velocity and mass of the ions in the electric wind in air. The London, Edinburgh, and Dublin Philosophical Magazine and Journal of Science, 48(294), 401-420.

[39] Plouraboué, F., “Flying with ionic wind,” Nature 563, 476 (2018).
[40] Lavigne, L., Zolghadri, A., Goupil, P., & Simon, P. (2008, December). Oscillatory failure case detection for new generation Airbus aircraft: a model-based challenge. In 2008 47th IEEE Conference on Decision and Control (pp. 1249-1254). IEEE.

APPENDIX

Appendix A. Pitot Tube Test Data Result Table

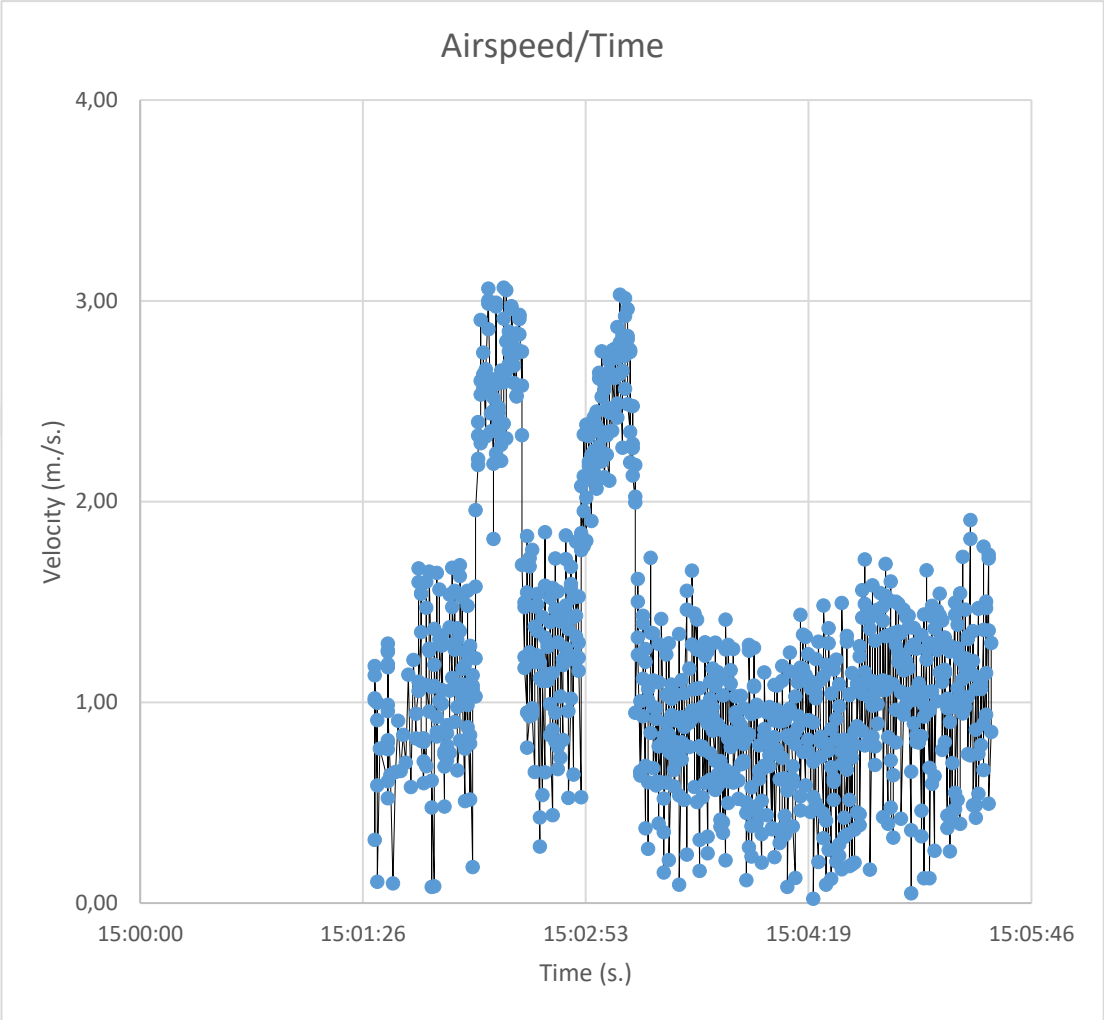

Appendix B. Python Script for Generating Graphs from Pitot Tube Test Data

```
import pandas as pd
import matplotlib.pyplot as plt
import matplotlib.dates as mdates
from datetime import datetime
url3 = " \\Test\\pito-tube-datas\\airspeedtest-3\\"
file_3 = "2024-04-30 16-13-22.txt"
l = []
with open(url3 + file_3, "r") as data:
   for line in data:
      line = line.rstrip()
      if "_vfr_hud_t airspeed" in line:
         parts = line.split()
         datetime_str = parts[0] + ' ' + parts[1]
         airspeed = parts[12].replace(",", ".")
         l.append([datetime_str, float(airspeed)])
df = pd.DataFrame(l, columns=['DateTime', 'Airspeed'])
df['DateTime'] = pd.to_datetime(df['DateTime'])
df_sampled = df.iloc[180::10]
std_dev = df_sampled['Airspeed'].std()
fig, ax = plt.subplots()
ax.errorbar(df_sampled['DateTime'], df_sampled['Airspeed'], yerr=std_dev, label='Airspeed SD',
fmt='-o', ecolor='red', capsize=3)
ax.xaxis.set_major_locator(mdates.SecondLocator(interval=15))  # frequency : 30 second
ax.xaxis.set_major_formatter(mdates.DateFormatter('%M:%S'))  # Saat:Dakika:Saniye
plt.title('Pito Tube Airspeed Test')
plt.xlabel('Time-min.:sec.')
plt.ylabel('Airspeed-m/s')
plt.xticks(rotation=45)
plt.legend()
plt.tight_layout()
plt.show()
```

Appendix C. Thrust Test Results for 12, 15 and 20 mm

12mm - 1				12mm - 2			
P	V	I	Thrust (N.)	P	V	I	Thrust (N.)
0.00	0.00	0.00	0.00E+00	0.00	0.00	0.00	0.00E+00
0.22	1.00	0.22	-9.81E-05	0.20	0.90	0.22	7.85E-05
0.33	1.10	0.30	-9.81E-05	0.24	1.00	0.24	1.96E-05
0.48	1.30	0.37	-9.81E-05	0.36	1.10	0.33	8.83E-05
0.72	1.60	0.45	-1.08E-04	0.47	1.20	0.39	9.81E-05
1.04	1.80	0.58	-1.96E-05	0.55	1.40	0.39	9.81E-05
1.20	1.90	0.63	8.83E-05	0.81	1.50	0.54	2.84E-04
1.44	2.00	0.72	5.89E-04	1.00	1.70	0.59	2.65E-04
1.70	2.10	0.81	6.08E-04	1.26	1.80	0.70	7.75E-04
1.83	2.20	0.83	1.03E-03	1.39	1.90	0.73	7.75E-04
2.07	2.30	0.90	1.08E-03	1.62	2.00	0.81	1.00E-03
2.28	2.40	0.95	1.15E-03	1.81	2.10	0.86	1.20E-03
2.53	2.50	1.01	1.17E-03	2.07	2.20	0.94	1.41E-03
2.86	2.60	1.10	1.81E-03	2.65	2.50	1.06	2.07E-03
2.97	2.70	1.10	1.81E-03	3.24	2.70	1.20	2.14E-03
3.42	2.80	1.22	1.87E-03	3.64	2.80	1.30	2.75E-03
3.63	2.90	1.25	2.42E-03	4.32	3.00	1.44	3.27E-03
3.90	3.00	1.30	2.43E-03	5.12	3.20	1.60	3.29E-03
6.05	3.10	1.95	4.02E-03	7.46	3.30	2.26	4.70E-03
6.70	3.30	2.03	4.08E-03	8.02	3.40	2.36	5.32E-03
7.58	3.40	2.23	4.08E-03	8.47	3.50	2.42	5.36E-03
8.09	3.50	2.31	5.08E-03	9.14	3.60	2.54	5.79E-03
8.57	3.60	2.38	5.10E-03	9.40	3.70	2.54	6.37E-03
10.03	3.80	2.64	5.89E-03	10.18	3.80	2.68	5.82E-03
10.61	3.90	2.72	5.87E-03	10.96	4.00	2.74	6.28E-03

15mm - 1				15mm - 2			
P	V	I	Thrust (N.)	P	V	I	Thrust (N.)
0.00	0.00	0.00	0.00E+00	0.00	0.00	0.00	0.00E+00
0.20	0.90	0.22	1.08E-04	0.64	1.40	0.46	3.14E-04
0.23	1.00	0.23	3.04E-04	1.48	1.80	0.82	4.22E-04
0.44	1.30	0.34	3.04E-04	1.37	1.90	0.72	1.02E-03
0.90	1.60	0.56	3.04E-04	1.70	2.00	0.85	1.09E-03

0.99	1.70	0.58	1.19E-03	1.81	2.10	0.86	1.66E-03
1.18	1.90	0.62	1.29E-03	2.07	2.20	0.94	1.66E-03
1.54	2.00	0.77	1.66E-03	2.50	2.40	1.04	1.69E-03
1.68	2.10	0.80	1.68E-03	2.73	2.50	1.09	2.49E-03
1.87	2.20	0.85	2.19E-03	2.99	2.60	1.15	2.49E-03
2.40	2.40	1.00	2.29E-03	3.32	2.70	1.23	2.50E-03
2.63	2.50	1.05	2.84E-03	4.20	3.00	1.40	3.36E-03
2.78	2.60	1.07	2.87E-03	4.46	3.10	1.44	3.83E-03
3.28	2.80	1.17	2.87E-03	4.96	3.20	1.55	3.80E-03
3.90	3.00	1.30	3.77E-03	5.12	3.30	1.55	3.81E-03
4.22	3.10	1.36	3.94E-03	5.51	3.40	1.62	4.42E-03
4.45	3.20	1.39	4.19E-03	5.71	3.50	1.63	4.44E-03
4.75	3.30	1.44	4.21E-03	6.51	3.70	1.76	4.93E-03
5.44	3.40	1.60	4.97E-03	7.22	3.80	1.90	5.30E-03
6.55	3.50	1.87	5.85E-03	10.18	3.90	2.61	6.44E-03
9.29	3.70	2.51	7.32E-03	10.72	4.00	2.68	6.74E-03
9.77	3.80	2.57	7.35E-03	11.44	4.10	2.79	6.98E-03

20mm - 1				**20mm - 2**			
P	**V**	**I**	**Thrust (N.)**	**P**	**V**	**I**	**Thrust (N.)**
0.00	0.00	0.00	0.00E+00	0.00	0.00	0.00	0.00E+00
0.63	1.40	0.45	-6.87E-05	0.29	1.00	0.29	-1.23E-03
0.87	1.50	0.58	6.08E-04	0.55	1.30	0.42	-1.27E-03
1.04	1.60	0.65	6.08E-04	0.72	1.50	0.48	-1.27E-03
1.21	1.80	0.67	7.16E-04	1.00	1.70	0.59	-1.27E-03
1.27	1.90	0.67	7.75E-04	1.37	1.90	0.72	-1.27E-03
1.64	2.00	0.82	1.12E-03	1.76	2.10	0.84	-1.27E-03
2.02	2.30	0.88	1.12E-03	2.00	2.20	0.91	-3.43E-04
2.52	2.40	1.05	1.66E-03	2.23	2.30	0.97	4.02E-04
2.78	2.50	1.11	1.68E-03	2.96	2.60	1.14	5.98E-04
3.04	2.60	1.17	1.68E-03	3.40	2.70	1.26	2.55E-04
4.02	3.00	1.34	2.15E-03	3.83	2.90	1.32	1.02E-03
4.54	3.20	1.42	2.15E-03	4.05	3.00	1.35	1.08E-03
5.20	3.40	1.53	3.06E-03	4.77	3.20	1.49	1.03E-03
6.88	3.70	1.86	3.06E-03	5.44	3.40	1.60	1.03E-03
7.18	3.90	1.84	4.28E-03	6.40	3.70	1.73	2.02E-03

7.64	4.00	1.91	3.86E-03	6.84	3.80	1.80	2.34E-03
9.68	4.10	2.36	4.59E-03	7.28	4.00	1.82	2.55E-03
10.08	4.20	2.40	4.78E-03	8.28	4.10	2.02	3.11E-03
12.34	4.30	2.87	5.43E-03	8.53	4.20	2.03	3.13E-03
13.11	4.40	2.98	5.61E-03	9.07	4.30	2.11	4.28E-03

Appendix D. Output Current and Voltage Calculation Results for 12, 15, and 20 mm

12mm - 1					
A	m2/V-sec	m	gr.	Watt	V
I_output	μ	d	T	P_input	V_output
0.00E+00	2.10E-04	0.01	0.00	0.00	0.00E+00
1.40E-06	2.10E-04	0.01	0.01	0.22	1.57E+05
1.40E-06	2.10E-04	0.01	0.01	0.33	2.36E+05
1.58E-06	2.10E-04	0.01	0.01	0.48	3.05E+05
1.23E-06	2.10E-04	0.01	0.01	0.72	5.88E+05
2.80E-06	2.10E-04	0.01	0.02	1.04	3.73E+05
4.73E-06	2.10E-04	0.01	0.03	1.20	2.53E+05
1.37E-05	2.10E-04	0.01	0.08	1.44	1.05E+05
1.38E-05	2.10E-04	0.01	0.08	1.70	1.23E+05
2.15E-05	2.10E-04	0.01	0.12	1.83	8.48E+04
2.24E-05	2.10E-04	0.01	0.13	2.07	9.24E+04
2.36E-05	2.10E-04	0.01	0.14	2.28	9.65E+04
2.40E-05	2.10E-04	0.01	0.14	2.53	1.05E+05
3.54E-05	2.10E-04	0.01	0.20	2.86	8.09E+04
3.55E-05	2.10E-04	0.01	0.20	2.97	8.36E+04
3.66E-05	2.10E-04	0.01	0.21	3.42	9.34E+04
4.64E-05	2.10E-04	0.01	0.27	3.63	7.82E+04
4.66E-05	2.10E-04	0.01	0.27	3.90	8.38E+04
7.49E-05	2.10E-04	0.01	0.43	6.05	8.07E+04
7.60E-05	2.10E-04	0.01	0.43	6.70	8.82E+04
7.60E-05	2.10E-04	0.01	0.43	7.58	9.98E+04
9.38E-05	2.10E-04	0.01	0.54	8.09	8.62E+04
9.42E-05	2.10E-04	0.01	0.54	8.57	9.10E+04
1.08E-04	2.10E-04	0.01	0.62	10.03	9.28E+04
1.08E-04	2.10E-04	0.01	0.62	10.61	9.84E+04
1.08E-04	2.10E-04	0.01	0.62	11.44	1.06E+05
1.09E-04	2.10E-04	0.01	0.62	12.10	1.11E+05
1.22E-04	2.10E-04	0.01	0.70	12.86	1.06E+05
1.22E-04	2.10E-04	0.01	0.70	13.16	1.08E+05

12mm - 2					
A	m2/V-sec	m	gr.	Watt	V
I_output	µ	d	T	P_input	V_output
0.00E+00	2.10E-04	0.01	0.00	0.00	0
1.40E-06	2.10E-04	0.01	0.01	0.20	1.41E+05
3.50E-07	2.10E-04	0.01	0.00	0.24	6.86E+05
1.58E-06	2.10E-04	0.01	0.01	0.36	2.30E+05
1.75E-06	2.10E-04	0.01	0.01	0.47	2.67E+05
1.75E-06	2.10E-04	0.01	0.01	0.55	3.12E+05
5.08E-06	2.10E-04	0.01	0.03	0.81	1.60E+05
4.73E-06	2.10E-04	0.01	0.03	1.00	2.12E+05
1.38E-05	2.10E-04	0.01	0.08	1.26	9.11E+04
1.38E-05	2.10E-04	0.01	0.08	1.39	1.00E+05
1.78E-05	2.10E-04	0.01	0.10	1.62	9.08E+04
2.13E-05	2.10E-04	0.01	0.12	1.81	8.46E+04
2.52E-05	2.10E-04	0.01	0.14	2.07	8.21E+04
3.69E-05	2.10E-04	0.01	0.21	2.65	7.18E+04
3.82E-05	2.10E-04	0.01	0.22	3.24	8.49E+04
4.90E-05	2.10E-04	0.01	0.28	3.64	7.43E+04
5.83E-05	2.10E-04	0.01	0.33	4.32	7.41E+04
5.86E-05	2.10E-04	0.01	0.34	5.12	8.73E+04
8.38E-05	2.10E-04	0.01	0.48	7.46	8.90E+04
9.48E-05	2.10E-04	0.01	0.54	8.02	8.46E+04
9.56E-05	2.10E-04	0.01	0.55	8.47	8.86E+04
1.03E-04	2.10E-04	0.01	0.59	9.14	8.86E+04
1.14E-04	2.10E-04	0.01	0.65	9.40	8.27E+04
1.04E-04	2.10E-04	0.01	0.59	10.18	9.81E+04
1.12E-04	2.10E-04	0.01	0.64	10.96	9.79E+04

15mm - 1					
A	m2/V-sec	m	gr.	Watt	V
I	µ	d	T	P_input	V_output
0.00E+00	0.00021	0.015	0	0	0
1.41E-06	0.00021	0.015	0.01	0.198	1.40E+05
4.34E-06	0.00021	0.015	0.031	0.23	5.30E+04
4.34E-06	0.00021	0.015	0.031	0.442	1.02E+05
4.34E-06	0.00021	0.015	0.031	0.896	2.06E+05
1.69E-05	0.00021	0.015	0.121	0.986	5.82E+04
1.83E-05	0.00021	0.015	0.131	1.178	6.42E+04

2.37E-05	0.00021	0.015	0.169	1.54	6.51E+04
2.39E-05	0.00021	0.015	0.171	1.68	7.02E+04
3.12E-05	0.00021	0.015	0.223	1.87	5.99E+04
3.26E-05	0.00021	0.015	0.233	2.4	7.36E+04
4.06E-05	0.00021	0.015	0.29	2.625	6.47E+04
4.10E-05	0.00021	0.015	0.293	2.782	6.79E+04
4.10E-05	0.00021	0.015	0.293	3.276	7.99E+04
5.38E-05	0.00021	0.015	0.384	3.9	7.25E+04
5.63E-05	0.00021	0.015	0.402	4.216	7.49E+04
5.98E-05	0.00021	0.015	0.427	4.448	7.44E+04
6.01E-05	0.00021	0.015	0.429	4.752	7.91E+04
7.10E-05	0.00021	0.015	0.507	5.44	7.66E+04
8.34E-05	0.00021	0.015	0.596	6.545	7.84E+04
1.04E-04	0.00021	0.015	0.746	9.287	8.89E+04
1.05E-04	0.00021	0.015	0.749	9.766	9.31E+04
1.05E-04	0.00021	0.015	0.751	10.296	9.79E+04
1.12E-04	0.00021	0.015	0.797	10.84	9.72E+04

15mm - 2					
A	**m2/V-sec**	**m**	**gr.**	**Watt**	**V**
I	**μ**	**d**	**T**	**P_input**	**V_output**
0.00E+00	2.10E-04	0.02	0.00	0.00	0.00E+00
4.48E-06	2.10E-04	0.02	0.03	0.64	1.44E+05
6.02E-06	2.10E-04	0.02	0.04	1.48	2.45E+05
1.46E-05	2.10E-04	0.02	0.10	1.37	9.40E+04
1.55E-05	2.10E-04	0.02	0.11	1.70	1.09E+05
2.37E-05	2.10E-04	0.02	0.17	1.81	7.63E+04
2.37E-05	2.10E-04	0.02	0.17	2.07	8.74E+04
2.41E-05	2.10E-04	0.02	0.17	2.50	1.04E+05
3.56E-05	2.10E-04	0.02	0.25	2.73	7.66E+04
3.56E-05	2.10E-04	0.02	0.25	2.99	8.41E+04
3.57E-05	2.10E-04	0.02	0.26	3.32	9.30E+04
4.79E-05	2.10E-04	0.02	0.34	4.20	8.77E+04
5.46E-05	2.10E-04	0.02	0.39	4.46	8.18E+04
5.42E-05	2.10E-04	0.02	0.39	4.96	9.15E+04
5.43E-05	2.10E-04	0.02	0.39	5.12	9.42E+04
6.31E-05	2.10E-04	0.02	0.45	5.51	8.72E+04
6.34E-05	2.10E-04	0.02	0.45	5.71	9.00E+04
7.04E-05	2.10E-04	0.02	0.50	6.51	9.25E+04
7.56E-05	2.10E-04	0.02	0.54	7.22	9.55E+04

9.18E-05	2.10E-04	0.02	0.66	10.18	1.11E+05
9.62E-05	2.10E-04	0.02	0.69	10.72	1.11E+05
9.97E-05	2.10E-04	0.02	0.71	11.44	1.15E+05
20mm - 1					
A	**m2/V-sec**	**m**	**gr.**	**Watt**	**V**
I	**μ**	**d**	**T**	**P_input**	**V_output**
0.00E+00	2.10E-04	0.02	-0.01	0.00	0.00E+00
6.51E-06	2.10E-04	0.02	0.06	0.87	1.34E+05
6.51E-06	2.10E-04	0.02	0.06	1.04	1.60E+05
7.67E-06	2.10E-04	0.02	0.07	1.21	1.57E+05
8.30E-06	2.10E-04	0.02	0.08	1.27	1.53E+05
1.20E-05	2.10E-04	0.02	0.11	1.64	1.37E+05
1.20E-05	2.10E-04	0.02	0.11	2.02	1.69E+05
1.77E-05	2.10E-04	0.02	0.17	2.52	1.42E+05
1.80E-05	2.10E-04	0.02	0.17	2.78	1.55E+05
1.80E-05	2.10E-04	0.02	0.17	3.04	1.69E+05
2.30E-05	2.10E-04	0.02	0.22	4.02	1.75E+05
2.30E-05	2.10E-04	0.02	0.22	4.54	1.98E+05
3.28E-05	2.10E-04	0.02	0.31	5.20	1.59E+05
3.28E-05	2.10E-04	0.02	0.31	6.88	2.10E+05
4.58E-05	2.10E-04	0.02	0.44	7.18	1.57E+05
4.13E-05	2.10E-04	0.02	0.39	7.64	1.85E+05
4.91E-05	2.10E-04	0.02	0.47	9.68	1.97E+05
5.11E-05	2.10E-04	0.02	0.49	10.08	1.97E+05
5.82E-05	2.10E-04	0.02	0.55	12.34	2.12E+05
6.00E-05	2.10E-04	0.02	0.57	13.11	2.19E+05

20mm - 2					
A	**m2/V-sec**	**m**	**gr.**	**Watt**	**V**
I	**μ**	**d**	**T**	**P_input**	**V_output**
0.00E+00	2.10E-04	0.02	0.00	0.00	0.00E+00
-1.31E-05	2.10E-04	0.02	-0.13	0.29	-2.21E+04
-1.35E-05	2.10E-04	0.02	-0.13	0.55	-4.03E+04
-1.35E-05	2.10E-04	0.02	-0.13	0.72	-5.32E+04
-1.35E-05	2.10E-04	0.02	-0.13	1.00	-7.40E+04
-1.35E-05	2.10E-04	0.02	-0.13	1.37	-1.01E+05
-1.35E-05	2.10E-04	0.02	-0.13	1.76	-1.30E+05
-3.68E-06	2.10E-04	0.02	-0.04	2.00	-5.45E+05
4.31E-06	2.10E-04	0.02	0.04	2.23	5.18E+05
6.41E-06	2.10E-04	0.02	0.06	2.96	4.63E+05

2.73E-06	2.10E-04	0.02	0.03	3.40	1.25E+06
1.09E-05	2.10E-04	0.02	0.10	3.83	3.51E+05
1.16E-05	2.10E-04	0.02	0.11	4.05	3.51E+05
1.10E-05	2.10E-04	0.02	0.11	4.77	4.32E+05
1.10E-05	2.10E-04	0.02	0.11	5.44	4.93E+05
2.16E-05	2.10E-04	0.02	0.21	6.40	2.96E+05
2.51E-05	2.10E-04	0.02	0.24	6.84	2.73E+05
2.73E-05	2.10E-04	0.02	0.26	7.28	2.67E+05
3.33E-05	2.10E-04	0.02	0.32	8.28	2.49E+05
3.34E-05	2.10E-04	0.02	0.32	8.53	2.55E+05
4.58E-05	2.10E-04	0.02	0.44	9.07	1.98E+05
4.60E-05	2.10E-04	0.02	0.44	13.11	2.85E+05

Appendix E. Speed and Speed Test Results

23.40 Watt			
Volt	Amper	time average	
10	2.34	0	Vel. (m/s)
start t		0	0
Tour Time		10	0
		14	0
		17	0
		20	0
		23	0
		26	0
		29	0

34.51-Watt Output			
Volt	Amper	time average	
11.90	2.9	7.25	Vel. (m/s)
start t		0	0
Tour Time	1.00	10	0.31
	1.50	14	0.39
	2.00	17	0.52
	2.50	20	0.52
	3.00	23	0.52
	3.50	26	0.52
	4.00	29	0.52

49.35-Watt Output			
Volt	Amper	time average	
14.10	3.5	9.00	Vel. (m/s)
start t		0	0
Tour Time	0.50	6	0.26
	1.00	11	0.31
	1.50	15	0.39
	2.00	18	0.52

68.88-Watt Output			
Volt	Amper	time average	
16.80	4.1	5.67	Vel. (m/s)
start t		0	0
Tour Time	0.50	4	0.39
	1.00	7	0.52
	1.50	10	0.52
	2.00	13	0.52
	2.50	15	0.79
	3.00	17	0.79

31.80-Watt Output			
Volt	Amper	time average	
5.30	6	4.86	Vel. (m/s)
start t		0	0
Tour Time	0.50	3	0.52
	1.00	6	0.52
	1.50	9	0.52
	2.00	11	0.79
	2.50	13	0.79
	3.00	15	0.79
	3.50	17	0.79